


5-1-2012

## Measured Rates of D2 Abstraction in H<sub>2</sub>O<sup>+</sup>, D<sub>2</sub> Substitution in H<sub>2</sub>DO<sup>+</sup> and Charge Transfer of He<sup>2+</sup> with Noble and Other Gases at <1eV

Chrysanthos Kyriakides  
University of Nevada, Las Vegas, athos2373@yahoo.com

Follow this and additional works at: <https://digitalscholarship.unlv.edu/thesesdissertations>

 Part of the [Atomic, Molecular and Optical Physics Commons](#)

---

### Repository Citation

Kyriakides, Chrysanthos, "Measured Rates of D<sub>2</sub> Abstraction in H<sub>2</sub>O<sup>+</sup>, D<sub>2</sub> Substitution in H<sub>2</sub>DO<sup>+</sup> and Charge Transfer of He<sup>2+</sup> with Noble and Other Gases at <1eV" (2012). *UNLV Theses, Dissertations, Professional Papers, and Capstones*. 1586.

<https://digitalscholarship.unlv.edu/thesesdissertations/1586>

This Dissertation is protected by copyright and/or related rights. It has been brought to you by Digital Scholarship@UNLV with permission from the rights-holder(s). You are free to use this Dissertation in any way that is permitted by the copyright and related rights legislation that applies to your use. For other uses you need to obtain permission from the rights-holder(s) directly, unless additional rights are indicated by a Creative Commons license in the record and/or on the work itself.

This Dissertation has been accepted for inclusion in UNLV Theses, Dissertations, Professional Papers, and Capstones by an authorized administrator of Digital Scholarship@UNLV. For more information, please contact [digitalscholarship@unlv.edu](mailto:digitalscholarship@unlv.edu).

MEASURED RATES OF D<sub>2</sub> ABSTRACTION IN H<sub>2</sub>O<sup>+</sup> , D<sub>2</sub> SUBSTITUTION IN  
H<sub>2</sub>DO<sup>+</sup> AND CHARGE TRANSFER OF He<sup>2+</sup> WITH NOBLE AND OTHER  
GASES AT <1eV

by

Chrysanthos Kyriakides

Bachelor of Science  
Rutgers, The State University of New Jersey, New Brunswick  
1996

Master of Science  
University of Arizona, Tucson  
2000

A dissertation submitted in partial fulfillment  
of the requirements for the

**Doctor of Philosophy in Physics**

**Department of Physics and Astronomy  
College of Sciences  
The Graduate College**

**University of Nevada, Las Vegas  
May 2012**

© Copyright 2012



THE GRADUATE COLLEGE

We recommend the dissertation prepared under our supervision by

**Chrysanthos Kyriakides**

entitled

**Measured Rates of  $D_2$  Abstraction in  $H_2O^+$ ,  $D_2$  Substitution in  $H_2DO^+$  and Charge Transfer of  $He^{2+}$  with Noble and Other Gases at  $<1eV$**

be accepted in partial fulfillment of the requirements for the degree of

**Doctor of Philosophy in Physics**

Department Physics and Astronomy

Victor Kwong, Committee Chair

Stephen Lepp, Committee Member

Michael Pravica, Committee Member

Peter Shiue, Graduate College Representative

Ronald Smith, Ph. D., Vice President for Research and Graduate Studies  
and Dean of the Graduate College

**May 2012**

## ABSTRACT

by

Chrysanthos Kyriakides

Dr. Victor H. S. Kwong, Examination Committee Chair

Professor of Physics

University of Nevada, Las Vegas

Experimental determination of the rate coefficient values of deuterium abstraction in water ions and deuterium substitution in hydronium ions can improve the understanding of D/H in water at planetary atmospheres, cometary atmospheres, and interstellar medium. Using a cylindrical ion trap, (CIT) and time of flight (TOF) mass spectrometry, a number of measurements at energies below 1 eV have been performed. The deuterium abstraction rate coefficient in water ions,  $\text{H}_2\text{O}^+$ , and an upper limit for the hydrogen-deuterium substitution rate coefficient in monodeuterated hydronium ion,  $\text{H}_2\text{DO}^+$ , have been measured. Both the abstraction and substitution rates were obtained by monitoring the population of  $\text{H}_2\text{DO}^+$ .  $\text{He}^{2+}$  is present in solar winds and cosmic radiation. It is also the ash of nuclear fusion in fusion reactors. Its charge transfer rate coefficients with various neutrals can help explain observations in astronomy as well as aid in better understanding the cooling via charge transfer of a plasma confinement type fusion reactor. Using the same experimental facility, the charge transfer rate coefficient of  $\alpha$ -particles with a number of neutrals in various reactions was also measured. For the first time at an energy as low, the resonant charge transfer (RCT) of  $\alpha$ -particles,  $\text{He}^{2+}$ , with helium has been measured. Also

the rate coefficient of the sum of single and double charge transfer of  $\text{He}^{2+}$  with Ne, Ar, Kr, Xe,  $\text{H}_2$ ,  $\text{D}_2$ ,  $\text{CH}_4$ ,  $\text{N}_2$  and CO were measured. The rate coefficients for charge transfer were measured by recording the loss rate of  $\text{He}^{2+}$ .

## ACKNOWLEDGEMENTS

I would like to thank Dr. Victor H. S. Kwong for going above and beyond his duties as my academic advisor. This work would have never been completed without his insightful and adroit guidance as well as his unwavering support. I would also like to acknowledge Dr. Stephen Lepp, Dr. Michael Pravica, and Dr. Peter Shiue for their valuable feedback, as well as Dr. Andrew Cornelius for making the helium measurements possible. Many thanks are due to Bill O' Donnell and Brad Clarke for their help.

## TABLE OF CONTENTS

ABSTRACT .....	iii
ACKNOWLEDGEMENTS .....	v
LIST OF FIGURES .....	ix
LIST OF TABLES .....	x
CHAPTER 1 INTRODUCTION .....	1
Section I: Water Ion Deuterium Abstraction and Monodeuterated Hydronium Deuterium Substitution .....	1
Section II: $\alpha$ -particles Charge Transfer Reactions.....	3
Section III: Dissertation Overview .....	4
CHAPTER 2 THEORY .....	5
Section I: The classical Theory .....	5
Section II: Conclusions .....	10
CHAPTER 3 EXPERIMENTAL PROCEDURE .....	11
Section I: System Overview.....	11
Section II: Operation and Timing.....	13
CHAPTER 4 DEUTERIUM ABSTRACTION AND SUBSTITUTION: MEASURE- MENTS RESULTS AND DISCUSSION .....	18
Section I: Modeling The Reactions.....	18
Section II: Eliminating Contaminant Ions .....	20
Section III: Elastic Collision Induced rf Heating Losses .....	26
Section IV: Results Discussion .....	27
CHAPTER 5 $\text{He}^{2+}$ CHARGE TRANSFER: MEASUREMENTS AND DISCUS- SION .....	34
Section I: Measurement Overview.....	34
Section II: $\text{He}^{2+}$ -He Measurements .....	35
Section III: $\text{He}^{2+}$ With Ne, Ar, Kr and Xe .....	46
Section IV: $\text{He}^{2+}$ with $\text{H}_2$ , $\text{D}_2$ , $\text{CH}_4$ , $\text{N}_2$ and CO .....	51
CHAPTER 6 CONCLUSIONS .....	57
APPENDIX .....	59
List of Abbreviations .....	59
BIBLIOGRAPHY .....	60
CURRICULUM VITA .....	65



## LIST OF FIGURES

2.1	Various trajectories of the ion-neutral pair shown. Only those that bring the pair in close proximity lead to reactions with the limiting case being a stable circular orbit around each other. The maximum impact parameter, $b_0$ , at which a reaction will occur is also shown. . . .	7
3.1	The layout of the system used for this work. . . . .	12
3.2	The sequence of the triggering pulses and the devices enabled by those pulses. This diagram is not drawn to scale. A. The ion creation triggering pulses. B. DC bias potential on the cathode shown in solid line. (The zero potential level shown by the dotted line to distinguish bias polarity) . C. Ion ejection triggering pulses. Also shown duration of recorded signal time, $t$ , used to record the ion signal intensity. Time $t$ does not begin until time relaxation time $\Delta t = 40$ ms in the case of $\text{He}^{2+}$ charge transfer reactions has elapsed D. The rf trapping potential. E. The DC offset to rf trapping potential. Zero potential also shown as dotted line. F. Potential on one of the endcaps with, negative, pull potential shown (other endcap not shown). . . . .	14
3.3	The stability diagram with some ions of interest, plotted in terms of $a_z$ and $q_z$ . Only ions inside the area labeled stable are trapped. In this case $m/q=26$ is not trapped . . . . .	15
3.4	A TOF spectrum, ions identified by their $m/q$ . . . . .	17
4.1	The stability diagram with ions trapped under the deuterium abstraction and substitution measurement conditions. In all three conditions $f = 600$ kHz and $V_0 = 213$ V. In the upper set of ions $U_0 = -6.3$ V ions with $m/q = 16$ and lower are not trapped. In the lower line/collection of ions $U_0 = 30.8$ V Ions with $m/q=24$ and higher are not trapped. In the final and middle position $U_0 = 11.24$ V. After having ejected all the unwanted ions ions $m/q= 17$ through $m/q=23$ remain and interact with deuterium. . . . .	23
4.2	The TOF spectrum show under different trapping conditions. A. Trapping with using a single DC offset. B. Trapping using a triple DC offset. All ions are identified by their $m/q$ . . . . .	24
4.3	$\text{H}_3\text{O}^+$ population at different trap time with hydrogen. The intensity was normalized to correct for any fluctuations in water, cathode output and hydrogen pressure. Shown here is the intensity at a hydrogen pressure equal to highest deuterium pressure used for the abstraction/substitution measurement. The decay rate is at $0.004 \text{ s}^{-1}$ . . . . .	27
4.4	$\text{H}_2\text{DO}^+$ population at different trap times with deuterium at $2.75 \times 10^{-7}$ Torr. The intensity was normalized to correct for any fluctuations in water, cathode output, and deuterium pressure. The fit curve is described by equation (4.17). . . . .	28

4.5	The rates $r_{abs.}$ and $r_{decay}$ plotted against their corresponding deuterium number densities, (a)The abstraction rates against density number density the deuterium abstraction in $H_2O^+$ rate coefficient is the slope(b)The $r_{decay}$ plotted against their corresponding deuterium number densities, the rate coefficient of deuterium substitution in $H_2DO^+$ is the slope. The error bars represent statistical error in the signal. The intercept at $2.8 \pm 1.2 \times 10^{-3} s^{-1}$ is within the measured value of the leak rate at the highest pressure	30
4.6	The TOF spectrum shown at different trap times. $m/q=19$ decays and reappears again.	30
5.1	The TOF spectra shown under the trapping conditions used in this work. The time $t$ , is set at zero, or 40 ms after ion creation, under different combinations of $^3He$ and $^4He$ gases. A. Spectrum with only $^3He$ gas introduced in the chamber. B. Spectrum with $^3He$ and $^4He$ gas. C. TOF spectrum with $^4He$ gas only. Ions with $m/q > 2$ are not stored. Ions with $m/q=1$ are $H^+$ , Ions with $m/q=1.5$ can only be $^3He^{2+}$ . Not all $m/q=2$ ions are $^4He^{2+}$ some are $H_2^+$ . Also note that not all $^4He^{2+}$ ions originate from the resonant charge transfer reactions. Some of $^4He^{2+}$ ions, are produced via EII on $^4He$ gas as shown in spectrum C. The high value RP is also displayed by all three spectra	39
5.2	The stability diagram with some ions of interest, ion coordinates plotted in terms the trapping parameters used to optimize storing for $^3He^{2+}$ . Ions trapped under conditions “a”, “▼”, have $f = 1.44$ MHz, $V_0 = 87$ V and $U_0 = 7$ V. Ions trapped under conditions “b”, “▲”, have the same $V_0$ and $f$ , but $U_0 = 10.5$ V. Ions in group “c”, “■”, have $f = 1.473$ MHz $V_0 = 47$ V and $U_0 = 2.2$ V. Trapping conditions are applied as follows, “a” for 14.5 ms, “b” for 7.3 ms and “c” for the remainder of the time spend inside the trap.	41
5.3	The relative $^3He^{2+}$ signal intensity plotted against time and at various $^4He$ pressures. The full evolution of the $^3He^{2+}$ signal intensity at the lowest $^4He$ pressure shown in the inset graph with the extended range of time.	43
5.4	The decay rates of the $^3He^{2+}$ signal plotted against their corresponding number densities of $^4He$ . The error bars correspond to the statistical error of the signal intensity	43
5.5	The $^3He^{2+}$ decay rates plotted against their corresponding $^3He$ number densities.	44
5.6	The $^3He^{2+}$ ion population decay under different Ne pressures, (a), and the corresponding decay rates plotted against Ne number densities, (b).	47
5.7	The $^4He^+$ ion population decay under different Ne pressures, (a), and the corresponding decay rates plotted against Ne number densities, (b).	47
5.8	The $^3He^{2+}$ ion population decay under different Ar pressures, (a), and the corresponding decay rates plotted against Ar number densities, (b).	48
5.9	The $^4He^+$ ion population decay under different Ar pressures, (a), and the corresponding decay rates plotted against Ar number densities, (b).	49

5.10	The $^3\text{He}^{2+}$ ion shown in its third and last trapping condition c used to measure rate coefficients with the rest of noble and non noble gases. The two conditions, a and b, that preceded it were similar to the ones used in $^3\text{He}^{2+}$ -He interactions, figure 5.2. The default location c corresponds to $f=1.473$ MHz $V_0=57$ V and $U_0=3.3$ V. The new location c is used to investigate whether there is a location dependency in the rate coefficient and has $f=1.463$ MHz $V_0=90$ V and $U_0=6.87$ V. The gases used to repeat the measurement at the new c location are Kr and Xe. ....	50
5.11	The $^3\text{He}^{2+}$ ion population decay under different Kr pressures, (a), and the corresponding decay rates plotted against Kr number densities, (b).	50
5.12	The $^4\text{He}^+$ ion population decay under different Kr pressures, (a), and the corresponding decay rates plotted against Kr number densities, (b).	51
5.13	The $^3\text{He}^{2+}$ ion population decay under different Xe pressures, (a), and the corresponding decay rates plotted against Xe number densities, (b).	52
5.14	The $^4\text{He}^+$ ion population decay under different Xe pressures, (a), and the corresponding decay rates plotted against Xe number densities, (b).	52
5.15	The $^3\text{He}^{2+}$ ion population decay under different $\text{H}_2$ pressures, (a), and the corresponding decay rates plotted against $\text{H}_2$ number densities, (b).	53
5.16	The $^3\text{He}^{2+}$ ion population decay under different $\text{D}_2$ pressures, (a), and the corresponding decay rates plotted against $\text{D}_2$ number densities, (b).	54
5.17	The $^3\text{He}^{2+}$ ion population decay under different $\text{CH}_4$ pressures, (a), and the corresponding decay rates plotted against $\text{CH}_4$ number densities, (b). ....	54
5.18	The $^3\text{He}^{2+}$ ion population decay under different $\text{N}_2$ pressures, (a), and the corresponding decay rates plotted against $\text{N}_2$ number densities, (b).	55
5.19	The $^3\text{He}^{2+}$ ion population decay under different CO pressures, (a), and the corresponding decay rates plotted against CO number densities, (b). ....	55

## LIST OF TABLES

- 6.1 All the  $\text{He}^{2+}$  results performed in this work compared, whenever available, to results from the literature under similar energy range .  $\blacklozenge$  Double or resonant charge transfer only.  $\blacktriangle$  The sum of single and double charge transfer rate coefficients.  $\blackstar$  Single charge transfer only. . . . . 58

## CHAPTER 1

### INTRODUCTION

This work addresses two different sets of measurements. It is therefore divided in two parts. In the first part, the measurements involving water ions deuterium abstraction and monodeuterated hydronium ions deuterium substitution will be examined. In the second part the  $\alpha$ -particle charge transfer reactions and the measured results will be queried.

#### Section I: Water Ion Deuterium Abstraction and Monodeuterated Hydronium

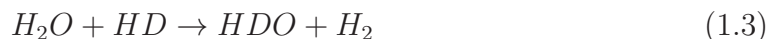
##### Deuterium Substitution

The deuterium abstraction in water ions as well as the deuterium substitution of hydronium ions are of importance in various aspects of astrophysics as well as planetary sciences. The deuterium abstraction deuterium and substitution reactions are:



Here, reaction (1.1) is the water ion abstraction and reaction (1.2) is the monodeuterated hydronium ion substitution. Water ions,  $\text{H}_2\text{O}^+$ , as well as hydronium ions,  $\text{H}_3\text{O}^+$ , were observed in the interstellar medium (ISM), [1, 2, 3, 4]. Studying the deuterium equivalent abstraction of  $\text{H}_2\text{O}^+$  to  $\text{H}_2\text{DO}^+$  and the subsequent substitution process of hydrogen by deuterium, can help understand and quantify the hydrogen

abstraction mechanism as deuterium is discernible from hydrogen and will play the role of a tag in the subsequent reactions. In addition to understanding the mechanism in hydrogen reactions, the actual isotopic reaction is present in the ISM given that deuteration of other molecular ion species,  $H_2^+$ ,  $HCO^+$ ,  $CH_3^+$  etc, was observed, modeled and studied[5, 6, 7, 8]. In comets the D/H ratio in water out gassing from their nuclei was found to be 10 times larger than the protosolar D/H ratio in  $H_2$ . [9, 10, 8]. A proposed process that can lead to that deuterium enrichment of water in comets is through ion molecule substitution reactions.[9, 11, 12]. The study of the Martian atmosphere revealed a much higher value for D/H ratio in water than the terrestrial ratio. In particular, the D/H ratio in water of the Martian atmosphere is up to six times higher[13, 14]. In previous models of the Martian atmosphere, even when a variety of potential escape mechanisms of  $H_2O$  from the Martian atmosphere are taken into account, leaving a higher concentration of deuterated water behind, the deuterium enrichment of water cannot be fully accounted [13]. Other studies, considered the substitution of hydrogen by deuterium through a neutral-neutral reaction as a mechanism to account for the deuterium enrichment of water in the Martian atmosphere:

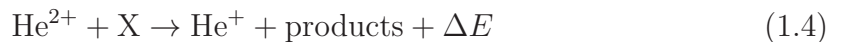


However the rate was found to be insufficiently slow. The neutral-neutral rate would have to be approximately ten orders of magnitude larger than the experimentally determined value to account for the observed D/H ratio discrepancy[13, 15]. A study of much faster ion-neutral reactions should also be considered to account for the isotopic enrichment and further enhance the understanding of the Martian atmospheric

composition. In addition to solar radiation, the Martian atmosphere is more susceptible than the earth to ionizing solar winds and cosmic radiation, given its weaker magnetic field. The higher production of ions, as compared to earth, in combination with the faster ion-neutral deuterium reactions may explain the difference in the D/H ratio in water in the two atmospheres and bridge the gap between observed and calculated water fractionation. Therefore, experimental determination of the deuterium abstraction and substitution in water ions and monodeuterated hydronium can help to better model and understand the various observed D/H ratios in water.

## Section II: $\alpha$ -particles Charge Transfer Reactions

Alpha-particles,  $\text{He}^{2+}$  ions, can be found in solar winds and cosmic radiation and are also the ash in nuclear fusion occurring in plasma confinement type reactors. They can charge transfer with most neutrals and the charge transfer reactions are given by:



Where X is any neutral species and reaction (1.4) is a single charge transfer and (1.5) is a double charge transfer reaction. The above charge transfer reactions are usually studied in the keV-MeV energy range, however, very little work exists in the 1-30 eV range [16]. The  $\alpha$ -particle charge transfer reactions with He,  $\text{D}_2$  and other neutrals found in the reactors, can be a cooling mechanism which can set a limit to the maximum plasma temperature at fusion reactors. That reduction

in maximum temperature makes the fusion conditions harder to reach [17]. The measured charge transfer of  $\text{He}^{2+}$  with neutrals such as  $\text{CO}$ ,  $\text{H}_2\text{O}$ ,  $\text{CO}_2$ ,  $\text{CH}_4$  found in cometary atmospheres, planetary atmospheres and the interstellar medium [18, 19, 20, 21], as well as He the second most abundant element in the universe, can also explain observed spectra in astrophysics. In this work, the gap that exists in measured charge transfer rate coefficients is filled. Values for charge transfer rate coefficients at energies between 0.24 eV to 0.40 eV are obtained experimentally. The neutrals used are He, for resonant charge transfer, as well as Ne, Ar, Kr, Xe,  $\text{H}_2$ ,  $\text{D}_2$ ,  $\text{CH}_4$ ,  $\text{N}_2$  and  $\text{CO}$ .

### Section III: Dissertation Overview

This work begins with a review of the theory of charge transfer, abstraction, and substitution reactions. An explanation of the experimental procedure and apparatus used in this dissertation follows. A more detailed experimental procedure, results, and discussion on isotopic abstraction and substitution in water and hydronium ions is contained in the next chapter. Concluding with the  $\text{He}^{2+}$  charge transfer measurements procedure, results and conclusions on the entirety of the work.



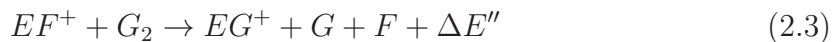
## CHAPTER 2

### THEORY

The theory behind charge transfer and isotopic abstraction and substitution will be discussed in this chapter. A full quantum mechanical treatment is needed to calculate cross sections of various reactions. However, it becomes quite involved as it requires solutions to complex Hamiltonian equations with multiple degrees of freedom. This is particularly challenging when considering interacting multi-atom and multi-electron neutrals and ions. No standardized equation exists and certain approximations are employed depending on the method applied in the quantum mechanical approach.

#### Section I: The classical Theory

Charge transfer reactions, abstraction reactions or substitution reactions can be written as:



Here reactions (2.1), (2.2), and (2.3) are charge transfer, abstraction, and substitution reactions respectively. In other words they involve the interaction of a neutral molecule or atom with an ion. In the classical model, both the neutral and ion are treated as finite spherical particles in order to calculate their cross section and rate

coefficient. This model was originally developed by Langevin and explored further by Gioumousis et al., and Su et al. [22, 23, 24, 25, 26]. Consider a spherical ion and a spherical neutral interacting. The long range potential between them can be described by  $\vec{p} \bullet \vec{E}$ . Where  $\vec{p}$  is the induced dipole moment and  $\vec{E}$  the electric field strength. The potential of the pair is therefore given by:

$$V_r = -\frac{q^2\alpha}{2r^4} \quad (2.4)$$

Here,  $\alpha$  is the polarizability of the neutral,  $q$  is the charge of the ion, and  $r$  is their internuclear separation. The two particles also have a scattering center displacement or impact parameter  $b$ , Figure 2.1. Reactions will occur so long as the pair spends enough time in close proximity to enable the reaction to happen. As the impact parameter is increased, the radius of the orbit of the one particle around the other will get larger. Reactions will proceed until a maximum value of the impact parameter  $b_0$  is reached. At  $b_0$ , a circular orbit is attained and adequate time is spent in proximity to allow the reaction to proceed. Any impact parameter greater than  $b_0$  means that the reaction will not proceed, as the trajectory does not allow for close proximity and adequate time for the reaction to happen, Figure 2.1.

The total energy of the pair is given by:

$$E_{total} = E_{kin.} - \frac{q^2\alpha}{2r^4} \quad (2.5)$$

Here,  $E_{kin.}$  is the kinetic energy of the system, and it is comprised of a rotational and a translational component. At infinite distance from each other the total energy

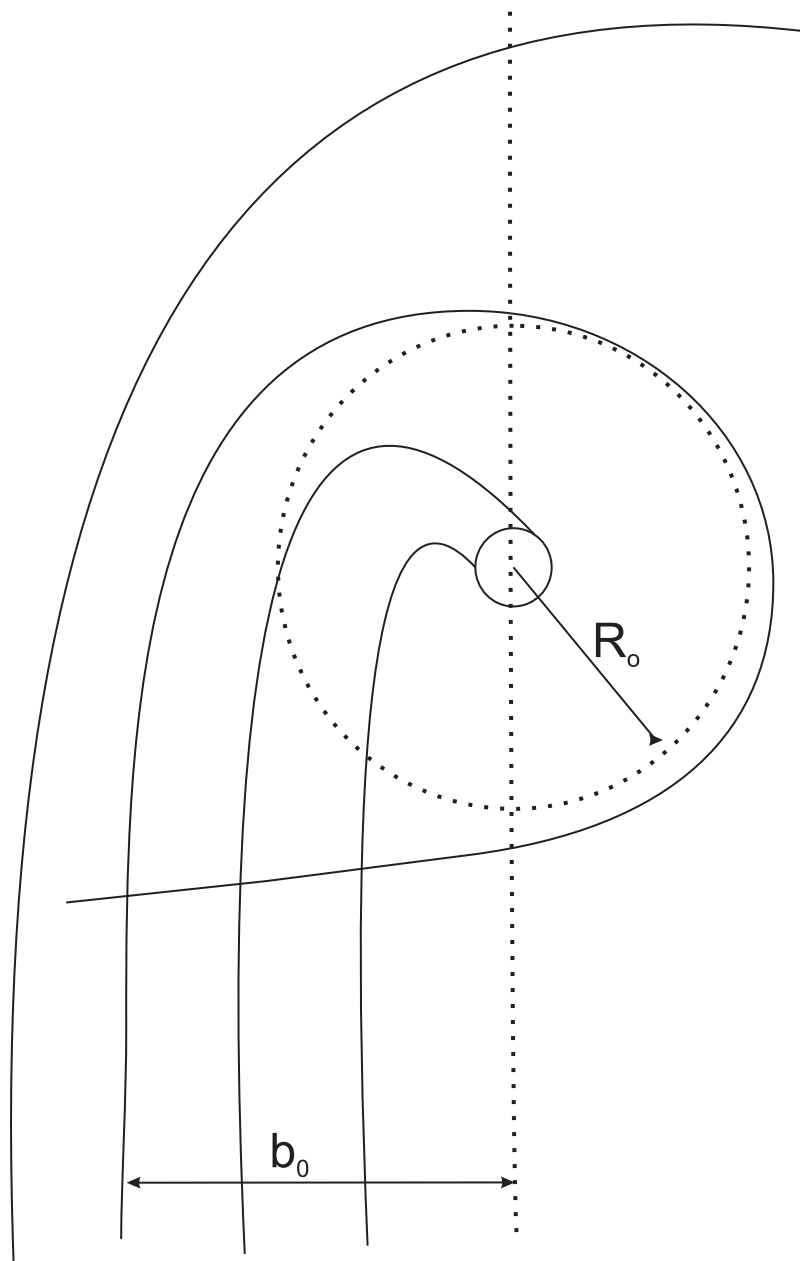


Figure 2.1: Various trajectories of the ion-neutral pair shown. Only those that bring the pair in close proximity lead to reactions with the limiting case being a stable circular orbit around each other. The maximum impact parameter,  $b_0$ , at which a reaction will occur is also shown.

of the pair is  $\frac{1}{2}\mu v^2$ , where  $\mu$  is the reduced mass of the pair, and  $v$  is the initial velocity. The rotational energy,  $E_{rot.}$ , can be written as:

$$E_{rot.} = \frac{L^2}{2\mu r^2} = \frac{\mu v^2 b}{2r^2} = \frac{E_{tot.} b^2}{r^2} \quad (2.6)$$

Where  $L$  is the angular momentum and is equal to  $\mu v b$ . Using the centrifugal potential associated with rotational energy, effective potential is:

$$V_{eff.} = \frac{L^2}{2\mu r^2} - \frac{q^2 \alpha}{2r^4} \quad (2.7)$$

Therefore, total energy can be rewritten as:

$$E_{total} = E_{trans.} + V_{eff.} \quad (2.8)$$

The parameter  $b_0$  is the maximum value of the impact parameter that would still yield a reaction. At  $b_0$ , the one particle will circle around the center of mass yielding the translational part of the kinetic energy as zero. In other words:

$$E_{total} = V_{eff.} = \frac{L^2}{2\mu r^2} - \frac{q^2 \alpha}{2r^4}$$

When the circular orbit is achieved, dipole attraction and rotational centrifugal forces are balanced. At the circular orbit the internuclear distance,  $r$ , is now  $R_0$ . To achieve the balance :

$$\frac{dV_{eff.}}{dr} = -\frac{L^2}{\mu r^3} + \frac{2q^2 \alpha}{r^5} = 0 \quad (2.9)$$

$$V_{eff.} = \frac{L^2}{2\mu r^2} - \frac{q^2\alpha}{2r^4} = E_{total} \quad (2.10)$$

Solving the equations (2.9) and (2.10), the following are obtained:

$$R_0 = \left(\frac{q}{b_0}\right) \left(\frac{\alpha}{E_{total}}\right)^{\frac{1}{2}} \quad (2.11)$$

$$b_0 = \left(\frac{2q^2\alpha}{E_{total}}\right)^{\frac{1}{4}} \quad (2.12)$$

The cross section can now be found. Since the reaction only happens up to the impact parameter,  $b_0$ , cross section  $\sigma$  is simply  $\pi b_0^2$ :

$$\sigma = \pi q \left(\frac{2\alpha}{E_{total}}\right)^{\frac{1}{2}} = \left(\frac{2\pi q}{v}\right) \left(\frac{\alpha}{\mu}\right)^{\frac{1}{2}} \quad (2.13)$$

The rate coefficient,  $k$  is simply  $\sigma v$  Therefore:

$$k = 2\pi q \left(\frac{\alpha}{\mu}\right)^{\frac{1}{2}} \quad (2.14)$$

Which is the Langevin rate coefficient. Su et al. [24, 25, 26] expanded this model to include polar molecules as well. Polar molecules, such as water, already have a permanent dipole moment that needs to be taken into account when considering  $V_{eff.}$ . Using the average dipole orientation (ADO) theory developed by Su et al. equation (2.10) can be rewritten as:

$$V_{eff.} = \frac{L^2}{2\mu r^2} - \frac{q^2\alpha}{2r^4} - \frac{q\mu_D}{r^2} \cos\bar{\theta}(r) \quad (2.15)$$

Where  $\mu_D$  is the dipole moment of the polar molecule and  $\bar{\theta}$  is the average orientation of the polar molecule's dipole with respect to line joining the center of the ion and neutral. A detailed treatment and an expression for  $k$  can be found elsewhere, [24, 25].

## Section II: Conclusions

The classical model is a good approximation for fast exoergic low energy reactions. Charge transfer cross sections at low energies, such as in this work, were described adequately by the classical model [27] and agreement was found with the quantum mechanical approach. Some of the charge transfer reactions of  $\text{He}^{2+}$  measured here were at or above the collisional rate as defined by equation (2.14). However, the classical model has its shortcomings since cross sections calculated under it have no dependency on temperature. The classical model fails to explain the magnitude of reactions such as isotopic substitution in hydronium. The quantum model is more apt for a more complete treatment and calculations of cross section and rate coefficients.

## CHAPTER 3

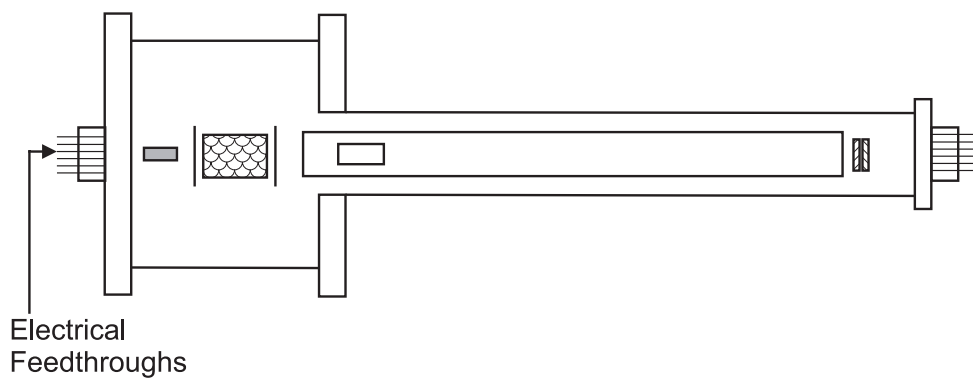
### EXPERIMENTAL PROCEDURE

#### Section I: System Overview

In order to accommodate the complex and difficult measurements performed, the system used for both sets of measurements is custom made and built in house . It consists of a dispenser barium oxide cathode, a cylindrical rf ion trap, a time of flight (TOF) drift tube, and a microchannel plate (MCP) all of which are housed in an ultra high vacuum (UHV) chamber, figure 3.1. The chamber is maintained at  $\approx 1 \times 10^{-11}$  Torr pressure which corresponds to approximately  $3.5 \times 10^5$  atoms per  $\text{cm}^{-3}$ . A Varian V-550 turbo molecular pump (TMP) backed by a two stage Alcatel rotary vane pump is used to reach UHV conditions. In addition a Masstror DX 100 quadrupole mass spectrometer (QMS) is used to monitor and measure the pressure of the various gases in the vacuum chamber. The cylindrical trap electrodes, ring electrode and flat endcaps are made from stainless steel 304 mesh. The ions are produced via electron impact ionization. The ions of interest are then stored inside the trap for a designated time where they are allowed to react with neutrals. Following that time expiration, ions are ejected, mass analyzed by the TOF drift tube, and detected by the MCP. The generated ion signal is displayed by a Tektronix TDS 680 C digital oscilloscope.

A detailed description of the facility used has been reported previously, [28]. The resolving power (RP),  $m/\Delta m$ , has been enhanced through major modifications to the facility, in some of which the author was involved. The modifications included the lengthening of the TOF drift tube from 25 cm to 48 cm with an electrostatic

## Chamber: Side View



## Chamber Interior: Side and Oblique views

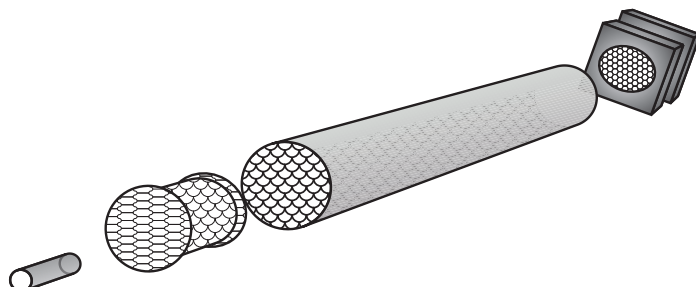
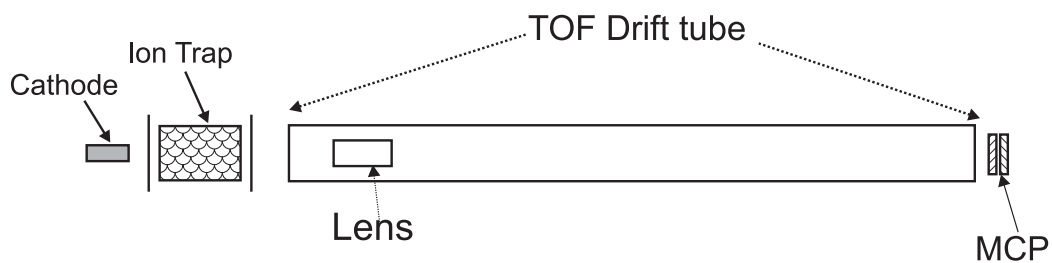


Figure 3.1: The layout of the system used for this work.



collimating lens, which was designed and built by the author, installed at its entrance. In addition modifications included the application of a short rise time push and pull pulses at the ion trap's end caps during the ion extraction to shorten the extraction time. These modifications resulted in a RP of 100 at  $m/q=20$ ,  $\text{H}_2\text{DO}^+$ , and 40 at  $m/q=1.5$ ,  ${}^3\text{He}^{2+}$ .

## Section II: Operation and Timing

The ions of interest are produced via electron impact ionization (EII) on neutrals that either originate from a gas reservoir, He, in the case of  $\alpha$ -particles, or are part of the residual gases, water, used for deuterium abstraction and substitution. The impacting electrons are produced continuously in a dispenser cathode. The flow of electrons from the cathode to the trap is controlled through the application of the appropriate DC bias, see B in figure 3.2. Electrons are confined on the cathode by the use of a positive bias DC potential. When the ion creation time is reached the ion creation trigger pulse, see A in figure 3.2, causes the reversal of the cathode bias polarity and the ejection of the electrons from the cathode into the trap, see B in figure 3.2. The ejected electrons ionize any neutral gases present that can be ionized. The negative bias potential on the cathode is optimized accordingly for either the production  ${}^3\text{He}^{2+}$  ions, or  $\text{H}_2\text{O}^+$ .

The trap used in this work has a cylindrical geometry. The potential surfaces near the center of the trap approximate those produced by an ideal hyperbolic trap. The stable trajectories of stored ions in a periodic hyperbolic potential can be obtained from the solutions to the Mathieu equation. The two parameters,  $a_z$  and  $q_z$ , determine

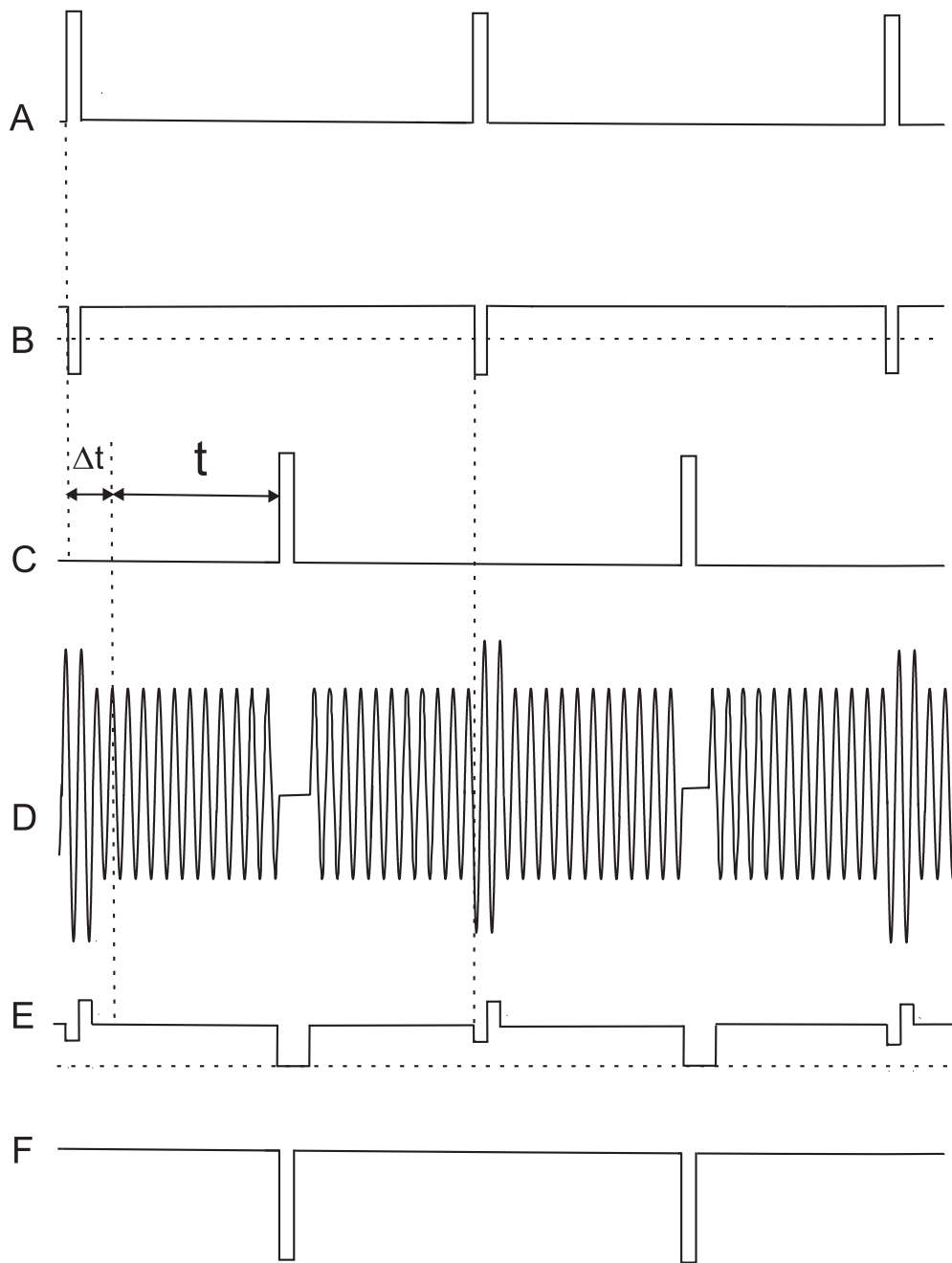


Figure 3.2: The sequence of the triggering pulses and the devices enabled by those pulses. This diagram is not drawn to scale. A. The ion creation triggering pulses. B. DC bias potential on the cathode shown in solid line. (The zero potential level shown by the dotted line to distinguish bias polarity) . C. Ion ejection triggering pulses. Also shown duration of recorded signal time,  $t$ , used to record the ion signal intensity. Time  $t$  does not begin until time relaxation time  $\Delta t = 40$  ms in the case of  $\text{He}^{2+}$  charge transfer reactions has elapsed D. The rf trapping potential. E. The DC offset to rf trapping potential. Zero potential also shown as dotted line. F. Potential on one of the endcaps with, negative, pull potential shown (other endcap not shown).

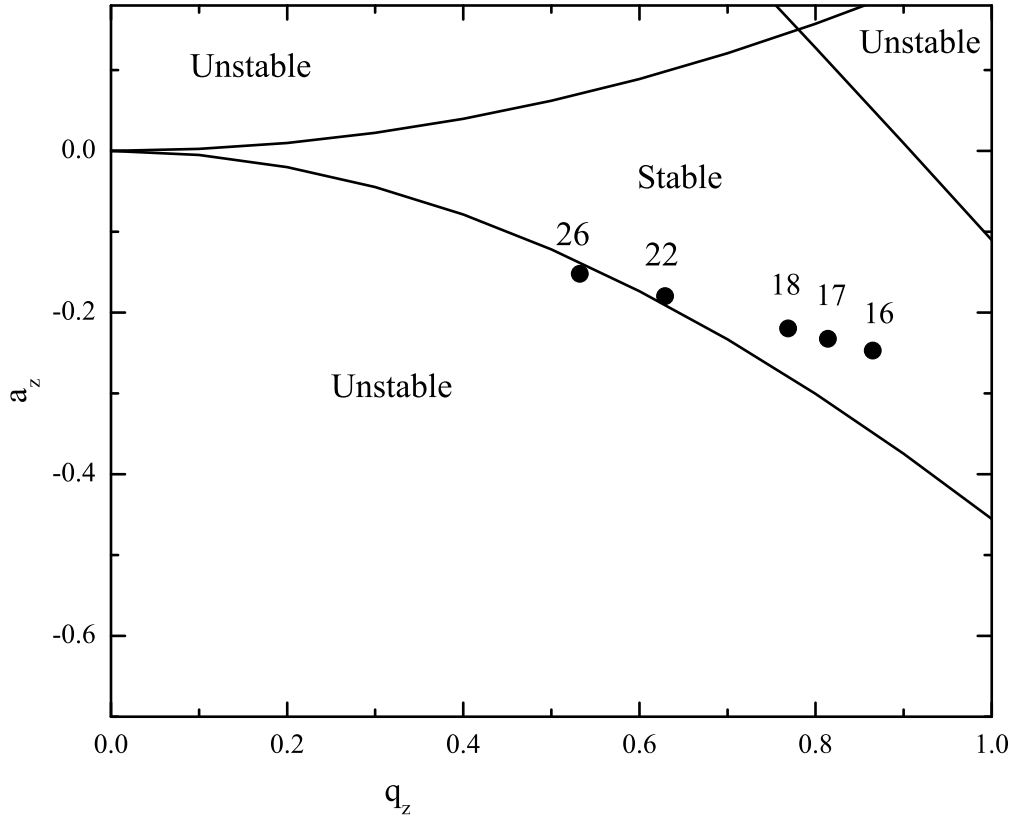


Figure 3.3: The stability diagram with some ions of interest, plotted in terms of  $a_z$  and  $q_z$ . Only ions inside the area labeled stable are trapped. In this case  $m/q=26$  is not trapped

whether an ion remains trapped inside the ion trap. Where:

$$a_z = \frac{-16qU_0}{m(r_0^2 + 2z_0^2)\Omega_0^2} \quad \text{and} \quad q_z = \frac{8qV_0}{m(r_0^2 + 2z_0^2)\Omega_0^2}$$

With  $V_0$ ,  $U_0$ ,  $\Omega_0$  are the rf potential's amplitude, DC offset and frequency respectively and  $r_0$ ,  $2z_0$  the trap's radius and length respectively. Only ions with  $a_z$  and  $q_z$  inside the stable region will remain confined in the ion trap, figure 3.3. The ion density distribution can be found in earlier work done on this trap [28].

While trapped the ions execute a motion that can be approximated as a three dimensional simple harmonic oscillator. In other words they behave as if they are

trapped in a pseudopotential well. The well's depth  $D_z$  and  $D_r$  in the axial and radial directions respectively are given by:

$$D_z = \left( \frac{4qV_0}{m(r_0^2 + 2z_0^2)\Omega_0^2} - \frac{2U_0}{(r_0^2 + 2z_0^2)\Omega_0^2} \right) z_0^2$$

$$D_r = \left( \frac{qV_0}{m(r_0^2 + 2z_0^2)\Omega_0^2} + \frac{U_0}{(r_0^2 + 2z_0^2)} \right) r_0^2$$

During the ejection of ions, the trapping potential, rf and DC offset, is turned off after the designated time expires. The rf and DC offset to the ring electrode, are grounded by a switch circuit triggered by the ion ejection trigger pulse, see C, D and E in Figure 3.2 . The ion ejection trigger pulse, C in Figure 3.2, also triggers the oscilloscope to initiate the TOF. To ensure complete extraction of the trap contents, into the TOF drift tube, the ion ejection trigger pulse simultaneously enables a DC push-pull type potential, at the trap's endcaps, see F in Figure. 3.2. Upon ejection from the trap, the ions are accelerated by a DC potential at -1400 V before entering the TOF drift tube for mass analysis. The TOF,  $T$ , is given by:

$$T = \sqrt{\frac{mL^2}{2qU}}$$

Where  $m$  and  $q$  are the ion's mass and charge respectively  $L$  the length of the drift tube and  $U$  the -1400 V potential. In other words, the sole factor that determines an ion's time of flight is its mass to charge ratio,  $m/q$ . The ions are detected by an MCP at the end of the TOF drift tube and a TOF spectrum is generated.

In the ion-signal collection stage the generated TOF spectrum, see figure 3.4, is

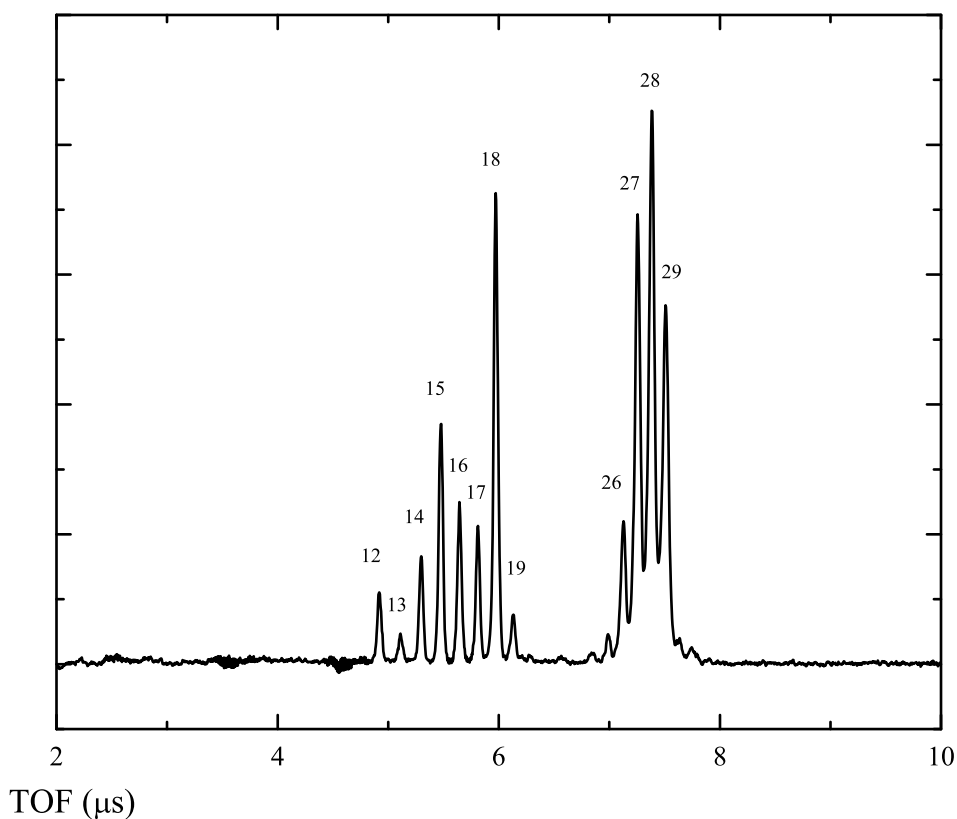


Figure 3.4: A TOF spectrum, ions identified by their  $m/q$

displayed on the oscilloscope while the digitized signal is recorded by a P.C.. The MCP is of chevron type is gated and set to activate 28 ms before the ion ejection pulse and stay on for 1 ms after the ions are ejected. The MCP potential is set to -1850V where it operates linearly, as it was shown experimentally in a separate measurement [29]. The gating of the MCP, protects it from the plethora of stray ions produced during ion creation. The 28 ms gating time is chosen to allow the MCP to reach a steady state potential of -1850V and produce the maximum signal. The area of the peak corresponding to the ion of interest is measured at various recorded signal times,  $t$ , and is averaged, using the recorded TOF spectrum, at 100 trials per time  $t$ .

## CHAPTER 4

### DEUTERIUM ABSTRACTION AND SUBSTITUTION: MEASUREMENTS RESULTS AND DISCUSSION

The measurement involving deuterium abstraction in water ions,  $H_2O^+$ , and deuterium substitution in singly deuterated hydronium ion,  $H_2DO^+$ , will be discussed in this chapter. The measurement of the abstraction and substitution rate coefficients are of importance to astrophysics and may help better model deuterium fractionation in water at planetary atmospheres, cometary atmospheres and ISM.

#### Section I: Modeling The Reactions

To understand the water and hydronium ions reactions with deuterium better the water/hydronium, ion reactions with hydrogen are considered. The water ions with hydrogen molecules reactions are well known and studied[30, 31, 32, 33]



Based on the hydrogen reactions a more complete list of the possible substitution and abstraction reactions, in addition to (1.1) and (1.2) given in chapter (1), would be:





The above reactions can be assigned in two groups of cascading decay type. The first group is made of reactions (4.2),(4.5) and (4.6) i.e.  $H_2O^+ \rightarrow H_2DO^+ \rightarrow HD_2O^+ \rightarrow D_3O^+$ . The second group comprises of reactions (4.3),(4.4), and (4.6) i.e.  $H_2O^+ \rightarrow HDO^+ \rightarrow HD_2O^+ \rightarrow D_3O^+$ . The substitution reaction (4.3) is not observed in this work. That can be explained when the magnitude of the rate of the substitution and abstraction reactions is taken into consideration. When the reactant ions,  $H_2O^+$ , interact with deuterium and have two possible routes available, the much faster abstraction route will dominate the substitution route. It is found in this work that abstraction rates are up to three orders of magnitude faster than substitution rates. Therefore the ions will always abstract whenever available. The second group does emanate from a substitution reaction,(4.3), which is competing against the first group's abstraction reaction,(4.2). The second group can therefore be eliminated as a possible route of reactions, since it is competing against a faster abstraction reaction. The final products of the deuterium reactions are hydronium ions, either fully or partly deuterated. When the first group of cascading reactions is considered,(4.2),(4.5)and (4.6), the growth or decay rates of the first abstraction type reaction (4.2) and the second substitution type reaction (4.5) can be written in the following differential equations:

$$\dot{N}_{H_2O^+} = -r_{abs}.N_{H_2O^+} \quad (4.7)$$

$$\dot{N}_{H_2DO^+} = r_{abs.}N_{H_2O^+} - r_{sub.}N_{H_2DO^+} \quad (4.8)$$

Where  $N_{H_2O^+}$  and  $N_{H_2DO^+}$ , refer to populations of  $H_2O^+$ ,  $m/q=18$ , and  $H_2DO^+$ ,  $m/q=20$ , respectively, The rates  $r_{abs.}$  and  $r_{sub.}$ , refer to the decay and growth rates of the population of  $H_2O^+$  respectively. The growth rate of  $H_2DO^+$  is caused by  $H_2O^+$  deuterium abstraction, and the decay rate by  $H_2DO^+$  deuterium substitution. Solving the differential equation (4.8) one gets:

$$N_{H_2DO^+} = \left( \frac{r_{abs.}N_{H_2O^+,0}}{r_{abs.} - r_{sub.}} \right) (e^{-r_{sub.}t} - e^{-r_{abs.}t}) \quad (4.9)$$

Where  $N_{H_2O^+,0}$  refers to the population of  $H_2O^+$  at time  $t = 0$ . By recording the time evolution of population  $N_{H_2DO^+}$ , i.e. the  $H_2DO^+$  ion population, the rates of abstraction for reaction (4.2) and substitution for (4.5) can be determined by double exponential curve fitting.

## Section II: Eliminating Contaminant Ions

The water ions were produced via EII and were a portion of the residual gas. The base pressure of the chamber never exceeded  $10^{-11}$  Torr however there were sufficient water molecules to be ionized and stored in the rf trap. No more than a few hundred are required to produce a strong ion signal. In fact, it was observed that exceeding a few thousand ions would saturate the detector and result to a “clipped” ion peak. The ions are stored in the rf trap and allowed to interact with deuterium anywhere from 160 ms to 19 seconds. Because of the erratic nature of the water molecule source



as well as fluctuations in the cathode output each trap time recorded is divided and normalized by a fixed trap time. In other words each trial recorded is paired with a normalization/reference trial. That measure is unavoidable and remedies the fluctuation in the signal intensity caused by cathode output fluctuations or water source output fluctuations.

An rf trapping potential at a given frequency and amplitude with a single DC offset value was used, originally. However, an rf potential with a single DC offset results in storing of unwanted ions. In addition to  $\text{H}_2\text{O}^+$ , EII, generates ions from other neutrals present in the residual gas, such as  $\text{CO}$ ,  $\text{CH}_3\text{OH}$ ,  $\text{C}_2\text{H}_5\text{OH}$ ,  $\text{C}_2\text{H}_2$ ,  $\text{CH}_4$  and other lighter hydrocarbons present in an ultra high vacuum system. A typical TOF mass spectrum of ions created by EII of residual gas and stored in the rf trap using a single DC offset is shown in figure 4.2. It is apparent that in addition to the desired  $\text{H}_2\text{O}^+$ ,  $m/q=18$ , other molecular ions including  $\text{CO}^+$ ,  $m/q=28$ ,  $\text{C}_2\text{H}_2^+$ ,  $m/q=26$ ,  $\text{OH}^+$ ,  $m/q=17$ ,  $\text{CH}_4^+$ ,  $m/q=16$ ,  $\text{CH}_3^+$ ,  $m/q=15$ ,  $\text{CH}_2^+$ ,  $m/q=14$ , and  $\text{CH}^+$ ,  $m/q=13$  are also stored. Since we have obtained the substitution and abstraction rate coefficients by measuring the time evolution of  $\text{H}_2\text{DO}^+$ ,  $m/q=20$ , population as described by eq. (4.9), any concomitant ions stored can contaminate the measurement, through production of  $\text{H}_2\text{O}^+$  and  $\text{H}_3\text{O}^+$  when reacting with deuterium and the residual gases.

$\text{CO}^+$  is produced by EII on residual  $\text{CO}$ . Carbon monoxide's ionization energy is close to  $\text{H}_2\text{O}$  and production of  $\text{CO}^+$  cannot be eliminated by any choice of the cathode's negative bias potential. The stored  $\text{CO}^+$ ,  $m/q=28$ , can react with residual  $\text{H}_2\text{O}$  to produce  $\text{H}_2\text{O}^+$  and  $\text{HCO}^+$ , [34, 35, 36]. In addition to the above,  $\text{CO}^+$  can produce  $\text{H}_2\text{DO}^+$  and  $\text{H}_2\text{O}^+$  through multiple steps with reactions with residual gases

and deuterium [32, 37, 38, 35, 36].  $C_2H_2^+$ ,  $m/q=26$ , reacts with residual gases and deuterium to produce  $H_2DO^+$  through two step processes [39, 40, 41, 42, 32] All other lighter hydrocarbon ions,  $CH_n^+$ , can react with residual water molecules to produce  $H_3O^+$ . The hydronium ion will subsequently react with  $D_2$  to produce  $H_2DO^+$ , [32].  $H_2O^+$  produced indirectly from sources other than EII and  $H_2DO^+$  originating either through deuteration of the indirectly produced  $H_2O^+$  or through reactions other than (4.2) will negate the validity of equation (4.9), on which equation our measurement is based. All these ions need to be excluded from the trap.

These offensive ions can be separated in two groups. Ions that are heavier than water ions,  $m/q=24$  and higher, and ions that are lighter than water ions, i.e. the lighter hydrocarbons. Instead of a single DC offset, a triple DC offset is employed to eliminate the unwanted contaminant ions and their subsequent products from the ion trap. During the first stages of ion creation, i.e. while the negative cathode bias is on for 10ms, a negative DC offset at -6.5 V is used for 14.5 ms, see Fig. 3.2 and Fig. 4.1. The negative offset ensures that lighter group of ions with  $m/q=16$  and lower are outside the stability diagram and therefore do not become trapped with the ions of interest. Following 14.5 ms of negative DC offset a positive DC offset at 30.8 V for approximately 7 ms is applied to the trap. That positive DC offset shifts the heavier group of ions with  $m/q=24$  and higher away from the stable region, see Fig. 4.1. These ions are therefore excluded from the trap. During the first two DC offset values,  $H_2O^+$ ,  $m/q=18$ , is safely inside the stability region. Finally a third DC offset with a value of 11.24 V is applied. The third DC offset, ensures that the ions of interest,  $H_2O^+$  and its abstraction product  $H_2DO^+$  now free of the unwanted ions,

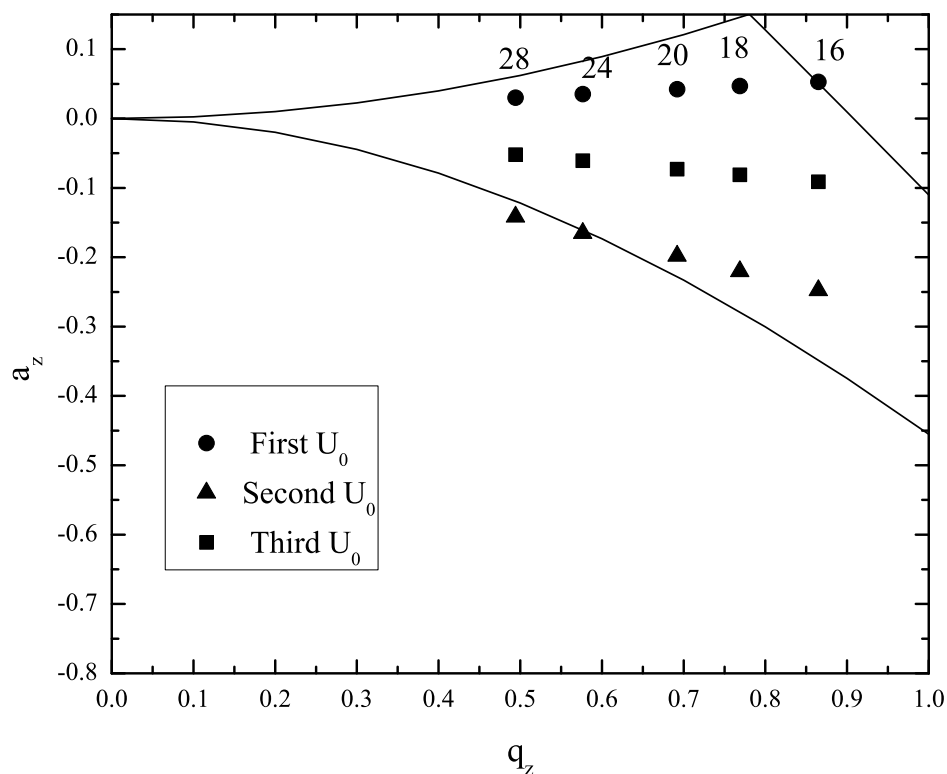


Figure 4.1: The stability diagram with ions trapped under the deuterium abstraction and substitution measurement conditions. In all three conditions  $f = 600$  kHz and  $V_0 = 213$  V. In the upper set of ions  $U_0 = -6.3$  V ions with  $m/q = 16$  and lower are not trapped. In the lower line/collection of ions  $U_0 = 30.8$  V Ions with  $m/q = 24$  and higher are not trapped. In the final and middle position  $U_0 = 11.24$  V. After having ejected all the unwanted ions ions  $m/q = 17$  through  $m/q = 23$  remain and interact with deuterium.

are trapped optimally. The effect of the triple DC offset in mass selection is shown in Fig. 4.2 .

Because of the  $\text{OH}^+$  and  $\text{H}_2\text{O}^+$   $m/q$  values proximity , it was not possible to eliminate  $\text{OH}^+$  without significantly reducing the  $\text{H}_2\text{O}^+$  signal. The deuteration reactions of  $\text{OH}^+$  are:



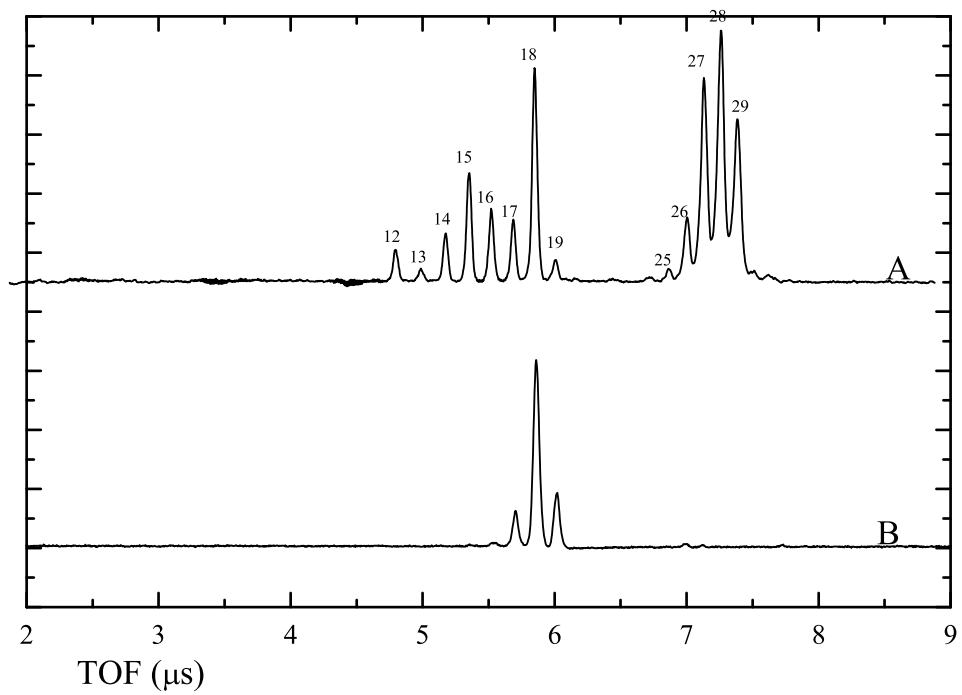
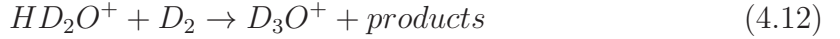


Figure 4.2: The TOF spectrum show under different trapping conditions. A. Trapping with using a single DC offset. B. Trapping using a triple DC offset. All ions are identified by their  $m/q$ .



The  $OH^+$  deuteration products “leap” over the  $H_2DO^+$  ions studied in this work. The deuteration chain leaves the  $m/q=20$  unaffected and the population of interest pure of any possible contaminants originating from  $OH^+$ . Reactions with neutrals, present in the residual gas, must also be considered, to completely exclude  $OH^+$  from a potential contamination source. The measurable neutrals found in the residual gas are CO,  $H_2O$ , as well as  $H_2$ .  $H_2$  is also part of the deuterium gas at 0.1% , as later scans indicated. The reactions are [43, 30]:



The most significant sources of contaminations would be reactions (4.13) and (4.16). Even though the rate coefficients of those reactions are high,  $1 \times 10^{-9} \text{cm}^{-3}$  and  $3 \times 10^{-9} \text{cm}^3 \text{s}^{-1}$  respectively, the number density of neutral reactants is low. The values of rate coefficients and number densities yield reaction rates that are hundreds of times smaller than the competing abstraction reactions of  $OH^+$  with deuterium, which have rate coefficient of the same order of magnitude. Therefore, the deuterium reactions will dominate and their products will not contaminate  $H_2DO^+$ . This makes the removal of  $OH^+$  unnecessary.

### Section III: Elastic Collision Induced rf Heating Losses

In addition to abstraction and substitution reactions other factors that affect the ion populations include collision induced rf heating losses, [44]. In this particular measurement the trapped ion is more massive than the interacting neutrals and collisional cooling will occur. In fact, Helium gas is used effectively to cool the trapped ions. However, some leaking will occur and given the small value of the substitution reaction the  $\text{H}_2\text{DO}^+$  ion losses from reasons other than deuterium substitution cannot be discounted. The Hydronium ion is used to evaluate and measure the leak rate. Hydronium ion,  $\text{H}_3\text{O}^+$ , is ideal for the leak test. It is very stable and it does not react with neutrals in the current residual gas, or ions in the trap. In addition to its invariance to reactions with ions trapped or neutrals present in the chamber, its mass to charge ratio of 19 is adjacent to the mass to charge ratio 20 of  $\text{H}_2\text{DO}^+$ . Those characteristics mean that with minor adjustments to the rf trapping potential's amplitude and the final DC offset, hydronium ion can be placed in the same stable coordinates,  $a_z$  and  $q_z$ , of  $m/q=20$ , which is the location of  $\text{H}_2\text{DO}^+$  in the stability diagram. That is the coordinates that are used for this work. If the hydronium ion signal decreases over time, no other reason for that decrease will exist other than hydronium ion leaking from the trap. In other words decrease in hydronium ion signal at  $\text{H}_2\text{DO}^+$  coordinates over time, means  $\text{H}_2\text{DO}^+$  at the trapping conditions for substitution/abstraction measurement will escape as well. In a separate measurement water ions are allowed to abstract with hydrogen gas and form  $\text{H}_3\text{O}^+$ . The reaction is given above (4.1) it is quite fast and has a value of  $\approx 8 \times 10^{-10} \text{cm}^3 \text{s}^{-1}$  [30, 31, 32, 33]. Hydronium itself does not react with hydrogen molecules a rate coefficient of  $\leq 10^{-15} \text{cm}^3 \text{s}^{-1}$

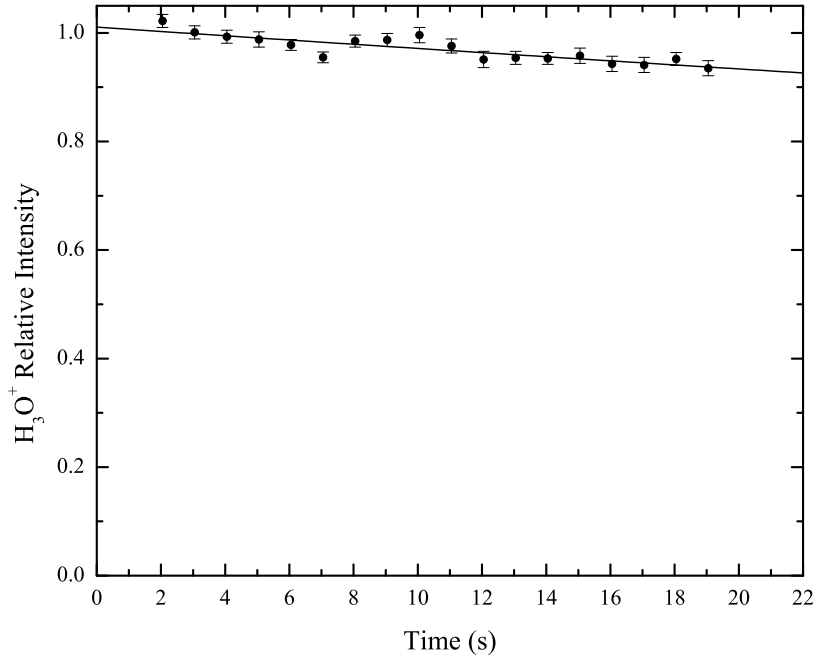


Figure 4.3:  $\text{H}_3\text{O}^+$  population at different trap time with hydrogen. The intensity was normalized to correct for any fluctuations in water, cathode output and hydrogen pressure. Shown here is the intensity at a hydrogen pressure equal to highest deuterium pressure used for the abstraction/substitution measurement. The decay rate is at  $0.004 \text{ s}^{-1}$

is given in the literature. [45]. A plot of the normalized signal intensity with respect to different trap times is given below, Fig. 4.3.

The value of the leak rate coefficient while it falls within the statistical error of the  $\text{H}_2\text{DO}^+$  growth rate caused by deuterium abstraction of  $\text{H}_2\text{O}^+$ , it is significant for the smaller value of the deuterium substitution in  $\text{H}_2\text{DO}^+$ . Therefore the effect of the leak due to elastic collision induced rf-heating on the deuterium substitution decay rate of  $\text{H}_2\text{DO}^+$  needs to be included.

#### Section IV: Results Discussion

Since normalization is used, to compensate for fluctuations in ion intensity, Equation (4.9) can be rewritten as:

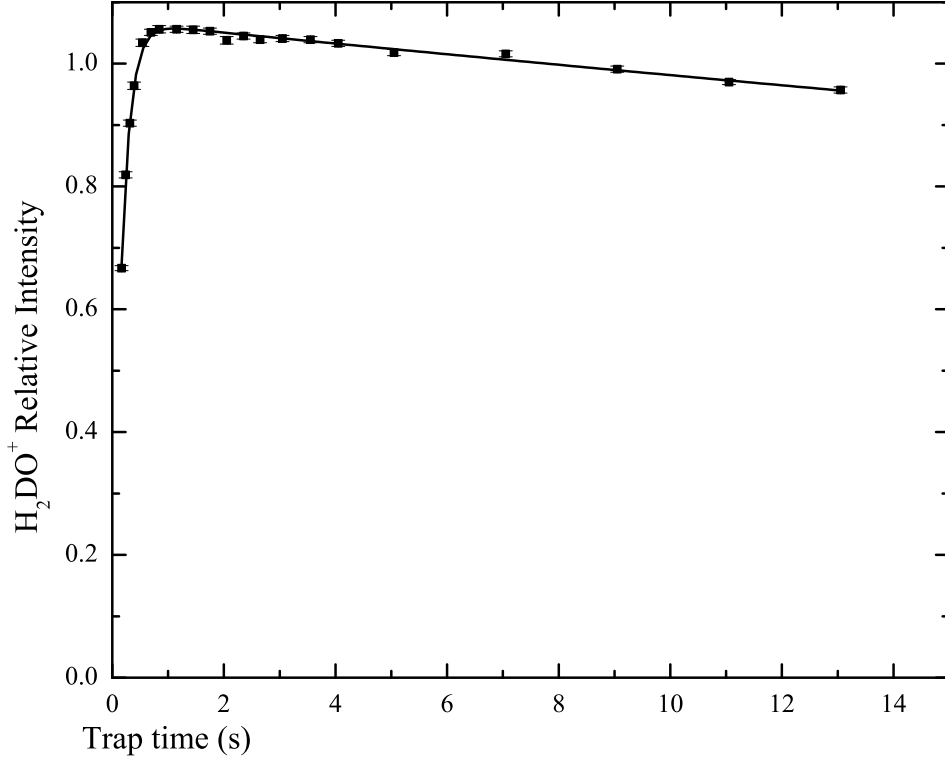


Figure 4.4:  $H_2DO^+$  population at different trap times with deuterium at  $2.75 \times 10^{-7}$  Torr. The intensity was normalized to correct for any fluctuations in water, cathode output, and deuterium pressure. The fit curve is described by equation (4.17).

$$I_{(H_2DO^+, t)} = C (e^{-(r_{sub.}+r_{leak})t} - e^{-r_{abs.}t}) \quad (4.17)$$

Where  $I_{(H_2DO^+, t)}$  is the normalized intensity of  $H_2DO^+$  and  $C$  is the normalization coefficient. The normalized intensity is recorded for up to twenty different trap times at 100 trials each. The process is repeated over six different deuterium pressures. A time evolution of the intensity is plotted and equation (4.17) is used for a least squares fit on the obtained profile.

The abstraction growth rate of  $H_2DO^+$  and the total decay rates,  $r_{abs.}$  and  $r_{sub.}+r_{leak}$  respectively, can be written as:



$$r_{abs.} = n_{D_2} k_{abs} \quad (4.18)$$

$$r_{decay} = r_{sub.} + r_{leak} = n_{D_2} k_{sub} + r_{leak} \quad (4.19)$$

Where  $n_{D_2}$  is the number density of deuterium gas in  $\text{cm}^{-3}$ ,  $k_{abs}$  and  $k_{sub}$  are the abstraction and substitution rate coefficients respectively in  $\text{cm}^3\text{s}^{-1}$ . The rate  $r_{leak}$  refers to losses of  $m/q=20$  signal that are caused by elastic collisions. As shown in figure 4.3 even at the highest pressure the leak rate, due to elastic collisions, is barely measurable. Therefore, for this measurement the leak rate is treated as a constant throughout various deuterium pressures. Since pressures are very low, the ideal gas law can be applied and deuterium number density,  $n_{D_2}$ , can be found. A least squares fit of  $r_{abs.}$  and  $r_{decay}$  against their corresponding deuterium number densities yields the corresponding deuterium abstraction and deuterium substitution rate coefficients.

After including systematic errors from QMS calibration The values of the slopes found is  $5.76 \pm 0.74 \times 10^{-10} \text{ cm}^3 \text{ s}^{-1}$  for the abstraction rate coefficient and an initial value of  $5.88 \pm 1.50 \times 10^{-13} \text{ cm}^3 \text{ s}^{-1}$  for the substitution rate coefficient. Further analysis of the data leads to the discovery of potential contamination to the substitution measurement. It is found that  $m/q=19$  while initially decaying completely it reappears at longer trap times and in fact grows at longer trap times.

The reappearance and persistence of  $m/q=19$  can be problematic for the substitution measurement. The most populous ion species in the trap and potential source of  $m/q=19$  is  $H_2DO^+$ . A significant decay in  $H_2DO^+$ , caused by a process other than deuterium substitution, means that the decay rate  $r_{sub}$  in equation (4.17) will in fact

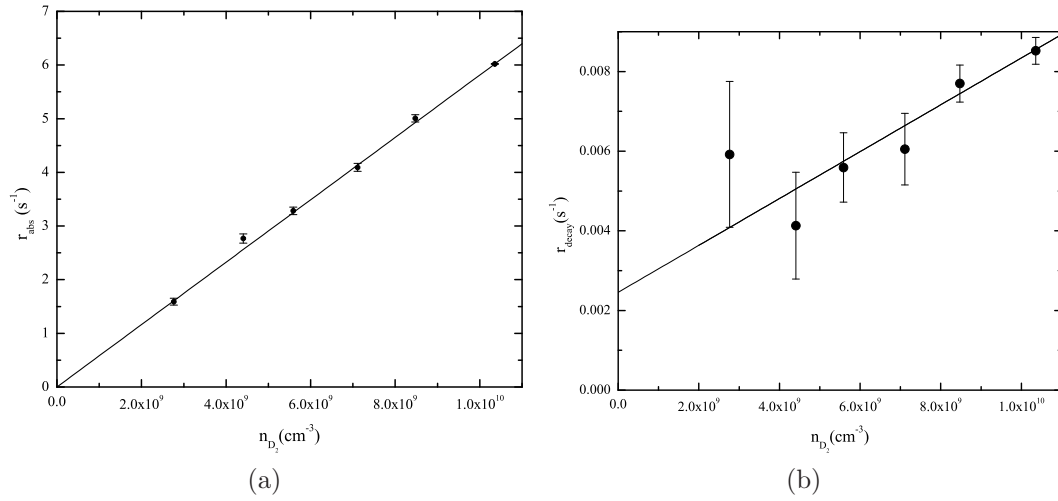


Figure 4.5: The rates  $r_{abs.}$  and  $r_{decay}$  plotted against their corresponding deuterium number densities, (a)The abstraction rates against density number density the deuterium abstraction in  $H_2O^+$  rate coefficient is the slope(b)The  $r_{decay}$  plotted against their corresponding deuterium number densities, the rate coefficient of deuterium substitution in  $H_2DO^+$  is the slope. The error bars represent statistical error in the signal. The intercept at  $2.8 \pm 1.2 \times 10^{-3} s^{-1}$  is within the measured value of the leak rate at the highest pressure

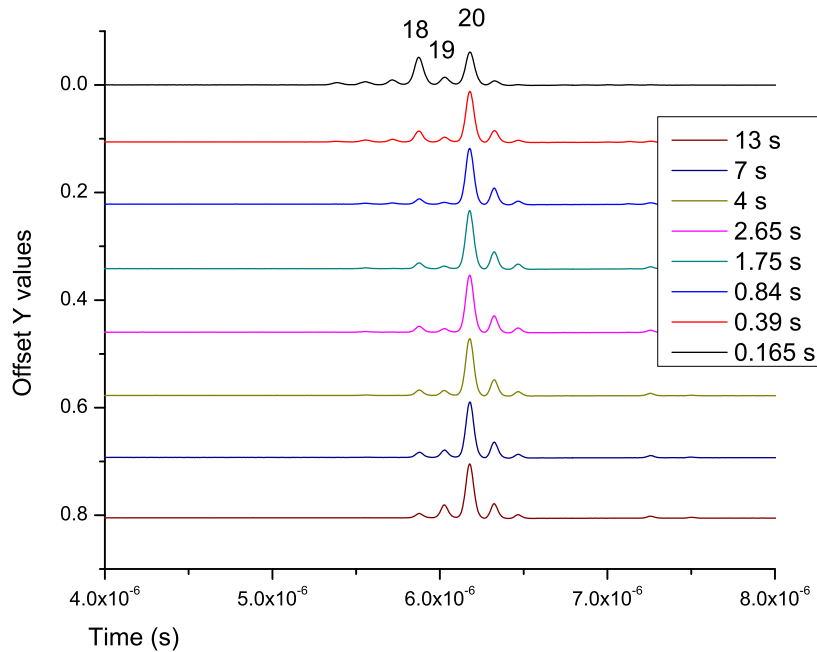


Figure 4.6: The TOF spectrum shown at different trap times.  $m/q=19$  decays and reappears again.

be a sum of that process along with the substitution i.e.

$$r_{decay} = n_{D_2}k_{sub} + n_xk_x + r_{leak} \quad (4.20)$$

Where x is the unknown contaminant and  $k_x$  the rate coefficient of that contaminating process. Therefore obtaining the substitution rate coefficient from the slope of a linear fit will be flawed as long as this process takes place. In an attempt to eliminate the contaminant it was essential to identify m/q=19. Its persistence over long trap times meant it is most likely  $H_3O^+$ .  $H_3O^+$  is a very stable ion as it was pointed out earlier. Its inertness will help explain its resilience in this case. It may have its hydrogens substituted by deuterium, which is present in great abundance during the experiment. However, as it is experimentally confirmed, substitution reactions are rather slow. This find also supports the longevity of  $H_3O^+$  at longer times. The next measure is to identify the process that decays  $H_2DO^+$  to  $H_3O^+$ . Possible reactions are:



The rate coefficient for reaction (4.21) is very fast,  $2 \times 10^{-9} \text{cm}^3 \text{s}^{-1}$  [46]. Reaction (4.22) is a substitution type reaction in a hydronium ion and even though no information is found. However, based on the experiment it is expected to be a slow process. Hydrogen exists in the gas but in very low numbers The rate coefficient

of (4.21) is substantially large and over three orders of magnitude larger than the  $\text{H}_2\text{DO}^+$  deuterium substitution rate coefficient. It would require a water number density of  $\approx 10^5 \text{cm}^{-3}$  to have comparable decay rates to the substitution. The last step to correct for this contamination is to eliminate or minimize the impact of the rogue reactions. Ionizing scans to evaluate water content in hydrogen or deuterium produce erroneous results. The QMS will yield erroneous results since it will actually produce water or heavy water when in contact with  $\text{D}_2$  or  $\text{H}_2$  gas [47]. Even though the QMS is off during the measurement and only used to scan gases at the beginning and end of sets, it is not possible to distinguish whether the high water concentration is a product of the QMS reaction, cathode by the ion trap reaction, or part of the deuterium gas used. To better assess the quality of the deuterium gas a non-ionizing gas chromatography scan is performed off site. The results indicated a clean gas with only 3.3 parts per million (ppm) of water/heavy water contents. Peak  $m/q=19$  persisted which means that the source of water has still not been eliminated. A closer look at the system, figure (3.1), reveals that the BaO is at close proximity to the ion trap. The hot cathode will continuously degas water. Given its proximity to the ions as well as the extended duration of ion storage, up to 19 seconds, the cathode is most likely the source of water. Therefore, the source of water cannot be eliminated and the measured deuterium substitution rate coefficient of  $5.88 \pm 1.50 \times 10^{-13} \text{ cm}^3 \text{ s}^{-1}$  is the upper limit of its value. The substitution rate coefficient is  $\leq 5.88 \pm 1.50 \times 10^{-13} \text{ cm}^3 \text{ s}^{-1}$ .

It is important to ensure that the values of rate coefficients obtained apply to the ground state of water molecules ions,  $\text{H}_2\text{O}^+$ . A potential mixture of ground

states and excited states of the above leads to uncertainty and unreliability in the rate coefficient values. As it was previously mentioned, water ions are produced via EII. The cathode produced the ionizing electrons at 109 eV. Electrons impacting at those energy levels do lead to excitation of water ions to higher electronic states. Initially, the majority of the water ions will be at the first and second excited state[48]. However, the second excited state is very short lived and it quickly transitions,  $10^{-14}$ s, to the first excited state [49]. In turn the first excited electronic state transitions to the ground electronic state measures in  $\leq 10\mu\text{s}$  [50]. Therefore within the first few microseconds all the water ion molecules will be at the ground electronic state. The first microseconds are of no consequence to the measurement, as can be seen by the plots, Fig. 4.4. Therefore, all the abstraction reactions materialized when the water ions are at their ground electronic state. The excited vibrational levels at the ground electronic state exhibit long radiative lifetimes with the longest being the first excited vibrational level, (0,1,0), of the second vibronic bending mode at 23 ms [51, 52]. A sizable number of water ions that are at the ground electronic state, either produced directly or through transitions from excited electronic states, will be at excited vibronic states [51]. However, given the radiative lifetimes of those excited vibronic states,  $\leq 23$  ms, and the duration of shortest trapping time, 160 ms, it is unlikely for a significant number of water ions to be at the excited vibronic states when any abstraction measurement was recorded, including the shortest trap time. In conclusion all abstraction measurements are recorded at ground electronic and ground vibronic states.

## CHAPTER 5

### He<sup>2+</sup> CHARGE TRANSFER: MEASUREMENTS AND DISCUSSION

#### Section I: Measurement Overview

The experimental measurement of rate coefficients of charge transfer between He<sup>2+</sup> and various neutrals will be examined in this part of the dissertation. The charge transfer reactions are given by (1.4) and (1.5).



Where (1.4) and (1.5) are single and double charge transfer respectively. The fact that the only factor determining an ion's TOF, and ergo its identification in the produced spectrum, is its  $m/q$  makes it impossible to distinguish between <sup>4</sup>He<sup>2+</sup> and H<sub>2</sub><sup>+</sup>. Both <sup>4</sup>He<sup>2+</sup> and H<sub>2</sub><sup>+</sup> have an identical  $m/q = 2$  and therefore an identical TOF which renders these ions indistinguishable. This muddling of <sup>4</sup>He<sup>2+</sup> and H<sub>2</sub><sup>+</sup> necessitated the use of <sup>3</sup>He, instead of the much more abundant <sup>4</sup>He. In an early attempt by the author to measure the charge transfer rate coefficients using <sup>4</sup>He the results gave a strong indication that the  $m/q = 2$  was contaminated mostly by H<sub>2</sub><sup>+</sup>.

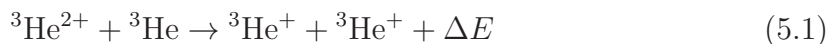
Using <sup>3</sup>He yields the <sup>3</sup>He<sup>2+</sup> ion with a unique  $m/q$  of 1.5 and a unique TOF. This solves the problem of contamination by H<sub>2</sub><sup>+</sup>. Because of their mass difference, <sup>3</sup>He and <sup>4</sup>He have a difference of ionization energy of about 1.1 meV ,[53]. However, it was found that the slight difference in ionization energy was negligible at 0.1 eV and

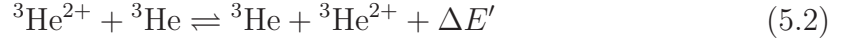
above [54]. Therefore the slight endoergicity of  ${}^3\text{He}$  with respect to  ${}^4\text{He}$  has no effect on measured rate coefficients at the energy levels I operate.

In all  $\text{He}^{2+}$  charge transfer measurements, and for any given trapping time, a fluctuation in the ion signal was observed. The  ${}^3\text{He}^{2+}$  ions, are extremely difficult to produce. They have a high ionization potential, 79 eV from neutral  ${}^3\text{He}$ , and small electron impact ionization cross section [55]. Additionally, although the cathode performed relatively consistently, it tends to fluctuate somewhat in its production of electron flux and electron energy. All of those factors contributed to a  ${}^3\text{He}^{2+}$  ion population and signal that fluctuated. To correct for those fluctuations, every recorded signal time, for a given neutral gas pressure, was accompanied by a fixed time reference signal. The area of the  ${}^3\text{He}^{2+}$  peak at a trap time to be used was averaged over 100 trials and then normalized by dividing it with the averaged area of the  ${}^3\text{He}^{2+}$  in the reference time. That normalization measure corrected very well and compensated for the factors mentioned above, which contributed to fluctuations in the ion signal. The reference time is chosen to be halfway between the two shortest trap times of the given pressure. As a result the reference time for the lowest gas pressure, for example, is chosen at 4 ms since the first two recorded signal times were 0 ms and 7 ms respectively. Other pressures are treated in a similar fashion

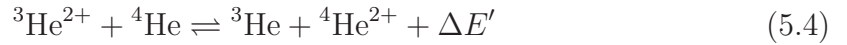
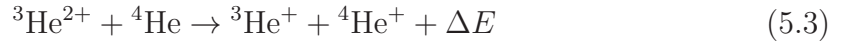
## Section II: $\text{He}^{2+}$ -He Measurements

When  ${}^3\text{He}$  reacts with  ${}^3\text{He}^{2+}$  reactions (1.4) and (1.5) can be rewritten as:





Where reaction (5.1) is the single charge transfer and (5.2) is the resonant charge transfer reaction. The resonant charge transfer reaction (RCT), has no effect on the ion population when both the ion and neutral are of the same isotope. Since the ion both on the right and on the left of (5.2) is of the same m/q, the ion population will remain unaffected by the RCT. Therefore, one can only measure the single charge transfer rate coefficient. However, when the ion and neutral are of different isotopes reactions (5.1) and (5.2) become:



The RCT does have an effect on  ${}^3\text{He}^{2+}$ . Since the produced,  ${}^4\text{He}^{2+}$  are of different m/q this causes a reduction in  ${}^3\text{He}^{2+}$  population and its resulting signal. Both of these pairs of reactions are used to determine single charge transfer (SCT) rate coefficient only, through use of the one He isotope, and both SCT and RCT rate coefficients through use of two different He isotopes. This measurement is performed by monitoring the depletion of the source,  ${}^3\text{He}^{2+}$ , not the products of the above charge transfer reactions. This set of measurements will begin by reporting on the  ${}^3\text{He}^{2+}$ - ${}^4\text{He}$  measurement followed by  ${}^3\text{He}^{2+}$ - ${}^3\text{He}$  and lastly a measurement to determine the rate coefficient of the leak rate caused by elastic collisions

As it was described in Chapter 3 all ions are produced via EII. In this particular case EII on neutral  ${}^3\text{He}$  atoms. The source of  ${}^3\text{He}$  atoms is a reservoir filled with



$^3\text{He}$  gas at 99.9% purity (Spectra Gases) and the atoms are introduced in the vacuum chamber through a leak valve. Other than  $^4\text{He}$ , that comprises 0.1% of the gas in the bottle, quadrupole mass spectrometer (QMS) scans of the gas indicated that the most dominant impurity is  $m/q=28$  at  $\approx 0.01\%$  followed by  $m/q=27$  at  $\approx 0.005\%$ . For the interactions with  $^4\text{He}$ ,  $^3\text{He}$  gas is maintained at a constant pressure of  $3.4 \times 10^{-8}$  Torr and is monitored through the QMS.

While the ions are trapped they interact with  $^4\text{He}$  originating from a separate leak valve and reservoir. The  $^4\text{He}$  reservoir is filled with 99.999% pure gas. (Praxair inc.) and its purity is confirmed by the QMS, Masstor DX 100, scans. To ensure that the direction of reaction (5.4) is from the left to right, the  $^4\text{He}$  pressure is varied from  $3.4 \times 10^{-7}$  Torr to  $2.1 \times 10^{-6}$  Torr or up to seventy times higher than the fixed  $^3\text{He}$  pressure. The ions spend a designated time, see C in Figure 3.2. Time  $t$ , recorded signal time, is varied and the signal intensity evolution is recorded. Time  $t$  can last up to 325 milliseconds. The relaxation time,  $\Delta t$ , at 40 ms, FIG. 3.2, is chosen to exceed the first two sets of transient trapping parameters that lasted  $\approx 23$  ms and to allow the  $^3\text{He}^{2+}$  to thermalize.

In addition to  $^3\text{He}^{2+}$ ,  $m/q=1.5$ , electron impact ionization generates ions from the gases emanating from the two reservoirs as well as other neutrals present in the residual gas.  $^3\text{He}^+$ ,  $m/q=3$ , and  $^4\text{He}^+$ ,  $m/q=4$ , are produced in greater numbers than  $^3\text{He}^{2+}$  given their larger ionization cross section. Additionally,  $^4\text{He}^{2+}$ ,  $\text{H}_2^+$ ,  $m/q=2$ ,  $\text{H}^+$ ,  $m/q=1$  are also produced. A variety of ions from water to light hydrocarbons, ions with  $m/q=12$  and higher, are also produced via ionization of neutrals present in an ultra high vacuum system. However any ion with  $m/q > 2$  cannot be stored, see

figure 5.2.

The ions other than  ${}^3\text{He}^{2+}$ , that remained stored, do not cause any contamination concerns to the charge transfer measurement.  $\text{H}^+$ ,  $m/q=1$ , or protons, and  ${}^4\text{He}^{2+}$ ,  $\text{H}_2^+$ ,  $m/q=2$ , do not react with fully stripped helium. The manipulation of ions in the stability diagram through the use of two different frequencies, two different rf amplitudes and three different DC offsets has the advantage that by eliminating  ${}^4\text{He}^+$  and  ${}^3\text{He}^+$  ions, figure 5.2, figure 5.1, the signal for  ${}^3\text{He}^{2+}$  becomes enhanced since now that it is not being displaced by the overabundance of singly charged helium ions. The sequence of the trapping parameters is applied in three stages. The first stage lasts 14.5 ms where its application commences at the rising edge of the ion creation pulse and exceeds the ion creation by 4.5 ms, the negative cathode bias is on for 10 ms. In the first stage the frequency is at 1.44 MHz the rf amplitude at 87 V and the DC offset at 7 V. Those trapping parameters will place  $\text{H}^+$  near the border of the stability diagram eliminating most of them, in addition some more energetic  ${}^3\text{He}^{2+}$  will also escape, see figure 5.2. In the second stage, the frequency and the rf amplitude are the same as in the first, however a higher DC offset at 10.5 V and for approximately 7.3 ms is applied to the trap. The higher DC offset shifted the group of ions with  $m/q=3$  and higher outside the stable region, see FIG. 5.2. Ions with  $m/q>2$  included the more abundant and readily produced  ${}^3\text{He}^+$  and  ${}^4\text{He}^+$  ions, which are ejected from the trap. During the first two stages,  ${}^3\text{He}^{2+}$ ,  $m/q=1.5$ , is safely inside the stability region. Finally in the third and final stage the frequency shifting key, FSK, is employed. At the end of the second set of trapping parameters and for the remainder of the time spent inside the trap, the frequency is shifted to 1.473 MHz. This shift in frequency is

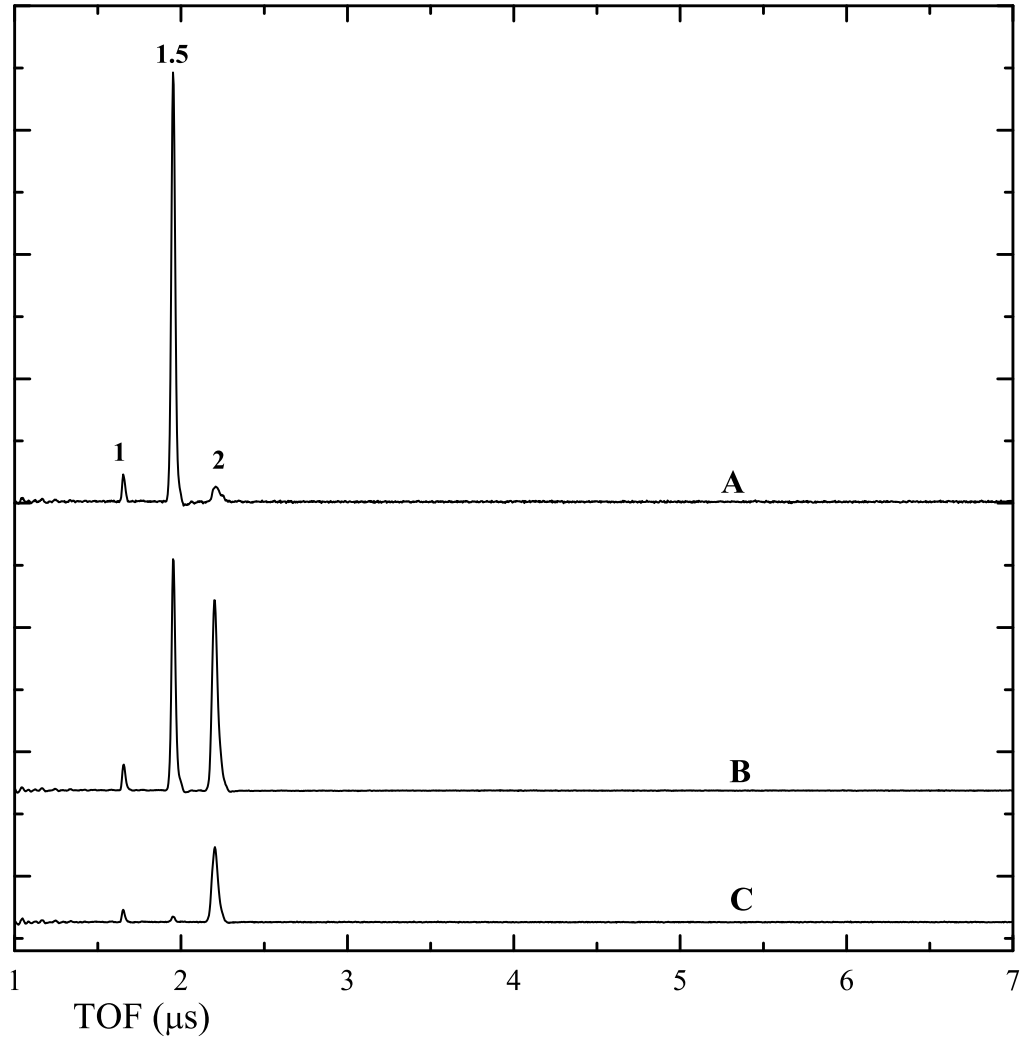


Figure 5.1: The TOF spectra shown under the trapping conditions used in this work. The time  $t$ , is set at zero, or 40 ms after ion creation, under different combinations of  $^3\text{He}$  and  $^4\text{He}$  gases. A. Spectrum with only  $^3\text{He}$  gas introduced in the chamber. B. Spectrum with  $^3\text{He}$  and  $^4\text{He}$  gas. C. TOF spectrum with  $^4\text{He}$  gas only. Ions with  $m/q > 2$  are not stored. Ions with  $m/q = 1$  are  $\text{H}^+$ , Ions with  $m/q = 1.5$  can only be  $^3\text{He}^{2+}$ . Not all  $m/q = 2$  ions are  $^4\text{He}^{2+}$  some are  $\text{H}_2^+$ . Also note that not all  $^4\text{He}^{2+}$  ions originate from the resonant charge transfer reactions. Some of  $^4\text{He}^{2+}$  ions, are produced via EII on  $^4\text{He}$  gas as shown in spectrum C. The high value RP is also displayed by all three spectra .

almost instantaneous, the transition takes  $< 1 \mu\text{s}$ , and it leads to a decrease in the rf amplitude to 47 V, see figure 3.2 and figure 5.2. The reduction in amplitude is caused by the frequency being off resonance with the LC, tank circuit connected to the ring electrode of the trap. A DC offset value at 2.2 V is applied at the third set. The third set of trapping parameters, ensures that the ion of interest,  ${}^3\text{He}^{2+}$ , now free of the unwanted ions, is trapped optimally. Using the pseudopotential well approximation, discussed in chapter 3 and developed earlier for the hyperbolic trap [56, 57], it is found that the ions of interest  ${}^3\text{He}^{2+}$ ,  $m/q=1.5$ , are trapped at an approximately spherical pseudopotential well with  $qD_z = qD_r = 2.4 \text{ eV}$  in the final set of trapping parameters. The trapped ions equilibrium temperature is approximately 1/10 of the value of the pseudopotential well depth [58, 59, 60]. Therefore, the trapped ions were at an energy of 0.24 eV or 0.08 eV/amu. The resulting TOF mass spectrum is shown in figure 5.1 .

The ion signal of the  ${}^3\text{He}^{2+}$  was recorded and its rate of depletion determined by varying the recorded signal times. The equation that describes the  ${}^3\text{He}^{2+}$  signal intensity  $N$  is given by

$$N_{(t)} = N_0 e^{-[n_{4\text{He}}k_{20} + n_{4\text{He}}k_{21} + n_b k_b + n_{4\text{He}}k_{\text{leak}}]t} \quad (5.5)$$

Where  $N_0$  is the  ${}^3\text{He}^{2+}$  population, at time  $t=0$ .  $n_{4\text{He}}$  refers to the  ${}^4\text{He}$  number density. Quantities  $k_{20}$  and  $k_{21}$  refer to the rate coefficients of RCT and SCT, reactions (5.4) and (5.3) .  $n_b$  is the background gases' number density and  $k_b$  their corresponding total charge transfer rate coefficient with  ${}^3\text{He}^{2+}$ . The  $k_{\text{leak}}$  quantity, is the rate coefficient of  ${}^3\text{He}^{2+}$  collision-induced rf driven ions loss [44]. In other words ions leaking out of the trap, without any charge transfer, through elastic collisions

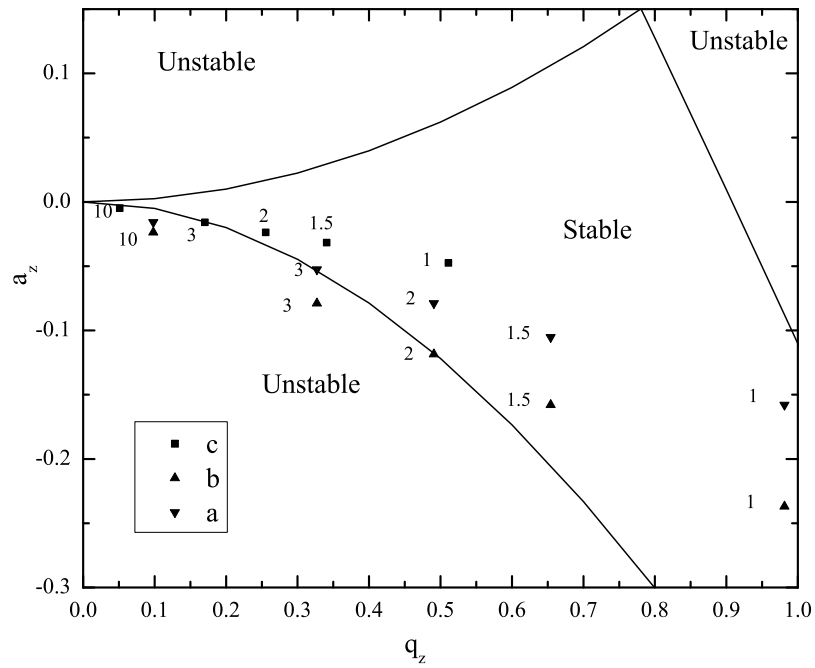


Figure 5.2: The stability diagram with some ions of interest, ion coordinates plotted in terms the trapping parameters used to optimize storing for  ${}^3\text{He}^{2+}$ . Ions trapped under conditions “a”, “▼”, have  $f = 1.44$  MHz,  $V_0 = 87$  V and  $U_0 = 7$  V. Ions trapped under conditions “b”, “▲”, have the same  $V_0$  and  $f$ , but  $U_0 = 10.5$  V. Ions in group “c”, “■”, have  $f = 1.473$  MHz  $V_0 = 47$  V and  $U_0 = 2.2$  V. Trapping conditions are applied as follows, “a” for 14.5 ms, “b” for 7.3 ms and “c” for the remainder of the time spend inside the trap.

with the most abundant gas,  $^4\text{He}$  and heating caused by the rf field. This phenomenon becomes more pronounced as the lighter trapped ion gains more energy through elastic collisions with more massive neutrals. The subsequent rf heating, from the applied rf trapping potential, leads to ion losses from the trap. It is mentioned above, that the  $^3\text{He}^{2+}$  signal intensity, is normalized to a reference intensity at fixed recorded signal time. Therefore, eq.(5.5) can be rewritten as:

$$N_{(t)} = Ae^{-[n_{4He}(k_{20}+k_{21}+k_{leak})+n_b k_b]t} \quad (5.6)$$

The decay rate at a given  $^4\text{He}$  pressure is obtained from a fit on the normalized ion signal intensity for a total of 14 different times. The process is repeated for six different pressures. With helium pressures not exceeding  $2.10 \times 10^{-6}$  Torr, the ideal gas law can be applied. Therefore, using the ideal gas law the six pressures can be translated to six number densities. The decay rates can be plotted against their corresponding number densities and a least squares fit can be performed. Since the decay rates,  $r$ , are given by:

$$r = n_{4He}((k_{20} + k_{21} + k_{leak}) + n_b k_b)$$

The slope is  $k_{20} + k_{21} + k_{leak}$  and the intercept  $n_b k_b$ . The value for the slope obtained was  $6.35 \pm 0.57 \times 10^{-10} \text{cm}^{-3} \text{s}^{-1}$ . It corresponds to the sum of the SCT, RCT and leak rate coefficients

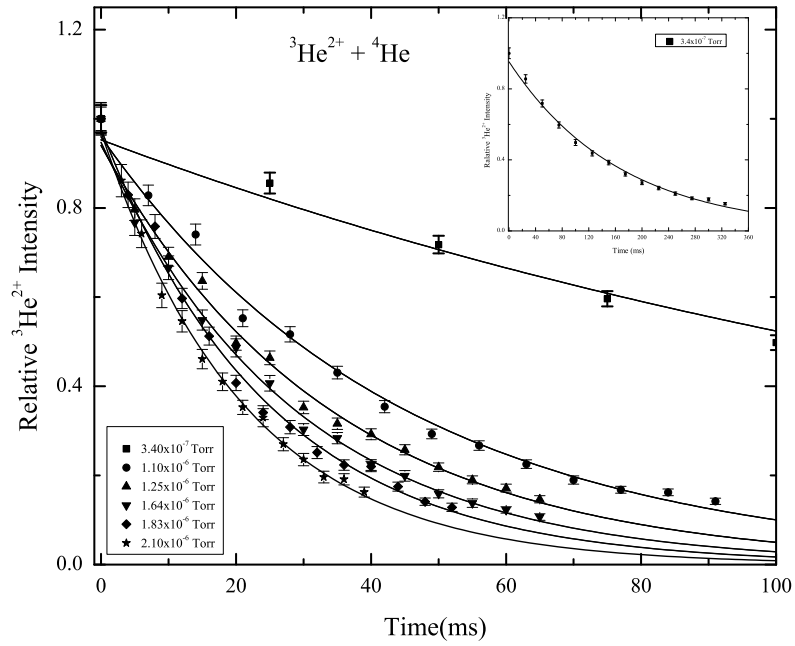


Figure 5.3: The relative  ${}^3\text{He}^{2+}$  signal intensity plotted against time and at various  ${}^4\text{He}$  pressures. The full evolution of the  ${}^3\text{He}^{2+}$  signal intensity at the lowest  ${}^4\text{He}$  pressure shown in the inset graph with the extended range of time.

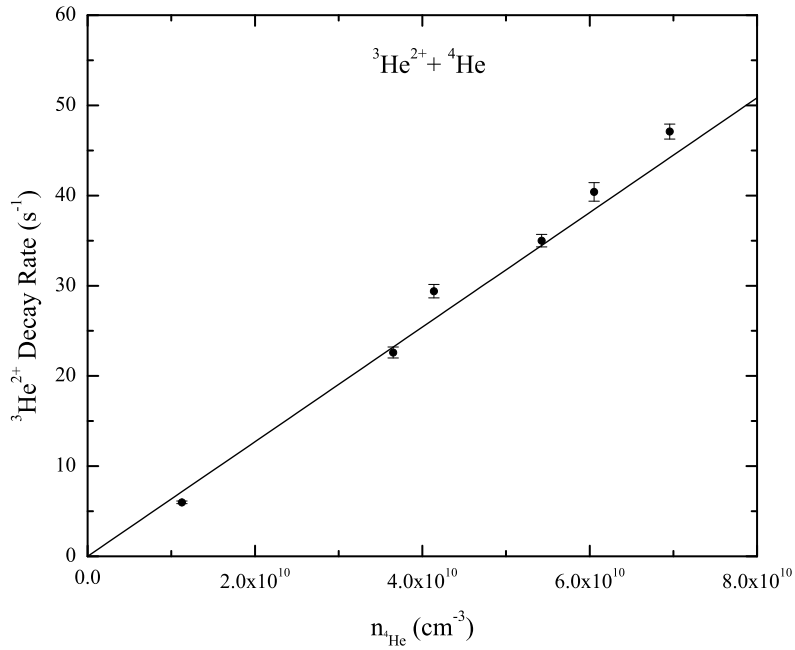


Figure 5.4: The decay rates of the  ${}^3\text{He}^{2+}$  signal plotted against their corresponding number densities of  ${}^4\text{He}$ . The error bars correspond to the statistical error of the signal intensity

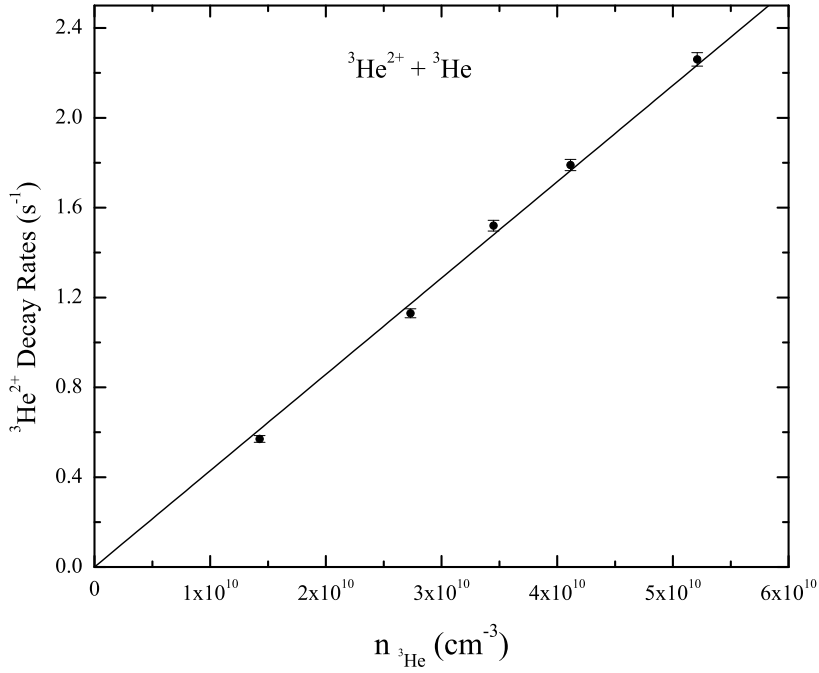


Figure 5.5: The  $^3\text{He}^{2+}$  decay rates plotted against their corresponding  $^3\text{He}$  number densities. .

As mentioned above to determine the RCT rate coefficient separately, the SCT and leak rate coefficients need to be determined in separate measurements. Succeeding the interactions of  $^3\text{He}^{2+}-^4\text{He}$  was a  $^3\text{He}^{2+}-^3\text{He}$  measurement. As explained above, by performing this measurement and recording the decay rates of the  $^3\text{He}^{2+}$  signal will yield the SCT and leak rate coefficients. This measurement is performed in a similar fashion to the  $^3\text{He}^{2+}-^4\text{He}$  measurement. Identical trapping conditions are applied but only a single isotope of helium was used. The rate coefficient obtained for this measurement was  $4.29 \pm 0.36 \times 10^{-11} \text{cm}^{-3} \text{s}^{-1}$

To evaluate the rate coefficient  $k_{leak}$  only, a separate measurement is also performed. To obtain a signal decay caused entirely by elastic collisions and emulate the conditions of  $^3\text{He}^{2+}$ ,  $^4\text{He}^+$  ions are produced and allowed to interact with  $^4\text{He}$ . The ion-neutral pair,  $^4\text{He}^+-^4\text{He}$ , is chosen because of the similar mass to the  $^3\text{He}^{2+}-^4\text{He}$



pair. Additionally, since the elastic collision cross section has an  $\alpha^{\frac{1}{2}}$  dependency [61], where  $\alpha$  is the polarizability of the neutral,  $^4\text{He}$  is the ideal candidate to evaluate the  $^3\text{He}^{2+}$  elastic collision induced rf heating ion leaks from the trap. Furthermore,  $^4\text{He}^+$  ions are inert with respect to  $^4\text{He}$  gas. Subsequently,  $^4\text{He}^+$  are not likely to have their signal intensity affected through charge transfer or any other reactions other than ejection from the trap through elastic collisions with  $^4\text{He}$ . To ensure the dimer ion,  $^4\text{He}_2^+$ , is not formed, a separate test is performed where no dimer with  $m/q = 8$  was detected. Unfortunately the rate obtained from this measurement is in the same range as the  $^3\text{He}^{2+}$ - $^3\text{He}$  measurement. This result can be interpreted as the SCT rate coefficient being orders of magnitude smaller than the leak rate coefficient caused by elastic collisions. Otherwise stated the  $^3\text{He}^{2+}$ , in the  $^3\text{He}^{2+}$ - $^3\text{He}$  measurement, escape the rf trap through collisions faster than they can singly charge transfer. The single charge transfer process does appear to be unhurried. In similar temperature conditions, the rate coefficient was previously measured and calculated at a value of  $4.8 \pm 0.5 \times 10^{-14} \text{ cm}^3 \text{ s}^{-1}$  [62, 63, 64].

The single charge transfer rate coefficient,  $k_{21}$ , can be dropped and the slope obtained from figure 5.4 can be rewritten as:

$$k_{20} + k_{leak}$$

The rate coefficient of RCT can be found by correcting the total rate coefficient or the slope value above for the leak rate coefficient. The corrected value of the RCT rate coefficient is  $5.92 \pm 0.58 \times 10^{-10} \text{ cm}^3 \text{ s}^{-1}$ . It is significantly fast and to the author's knowledge no experimental work at this energy level exists in the literature.

### Section III: He<sup>2+</sup> With Ne, Ar, Kr and Xe

The measurements of charge transfer rate coefficients of <sup>3</sup>He<sup>2+</sup> with the rest of the noble gases are also achieved through recording the depletion rate of <sup>3</sup>He<sup>2+</sup>. Because of that fact it is not possible to distinguish single and double charge transfer of <sup>3</sup>He<sup>2+</sup>, SCT and DCT, reactions (1.4) and (1.5), with the rest of the noble gases. The rate coefficients obtained are the sum of single and double charge transfer of <sup>3</sup>He<sup>2+</sup> with Ne, Ar, Kr and Xe. The set of trapping parameters, used for these measurements, were slightly different than the ones used in <sup>3</sup>He<sup>2+</sup>-He, see figure 5.2 . While the order and duration of each of the three sets of parameters is the same as in the helium charge transfer reactions the magnitudes of the rf amplitude and the DC offsets were different. Set a had f=1.44 MHz V V<sub>0</sub>=95 V U<sub>0</sub>=2.2V, set b has same f and V<sub>0</sub> as in a its U<sub>0</sub> is 15.8 V, finally set c has f=1.473 MHz, V<sub>0</sub>=57 V and U<sub>0</sub>=2.2V. The third and final trapping set positions <sup>3</sup>He<sup>2+</sup> at a qD<sub>z</sub>= 4.8 eV and qD<sub>r</sub>=3.4 eV. Meaning an energy of 0.34 eV for the ion based at the 1/10 of the shallowest qD value.

In charge transfer of <sup>3</sup>He<sup>2+</sup> with Ne, the gas used was of 99.999% purity (Praxair). QMS scans indicated that other than Ne isotopes the most appreciable gas was Ar isotopes m/q=40 with  $\approx 0.01\%$  concentration. The SCT, DCT as well as leak rate coefficients are obtained for the slope of <sup>3</sup>He<sup>2+</sup> signal loss rate as a function of Ne number density, figure 5.6.

The value obtained from the slope is  $1.37 \pm 0.16 \times 10^{-9} \text{cm}^{-3} \text{s}^{-1}$ . That value corresponds to the sum of DCT, SCT and leak rate coefficients,  $k_{20}$ ,  $k_{21}$  and  $k_{leak}$ , of <sup>3</sup>He<sup>2+</sup> with Ne. To obtain  $k_{leak}$  separately a different measurement using <sup>4</sup>He<sup>+</sup> and Ne is carried out. As in the <sup>4</sup>He<sup>+</sup> with He reaction, from the previous section,

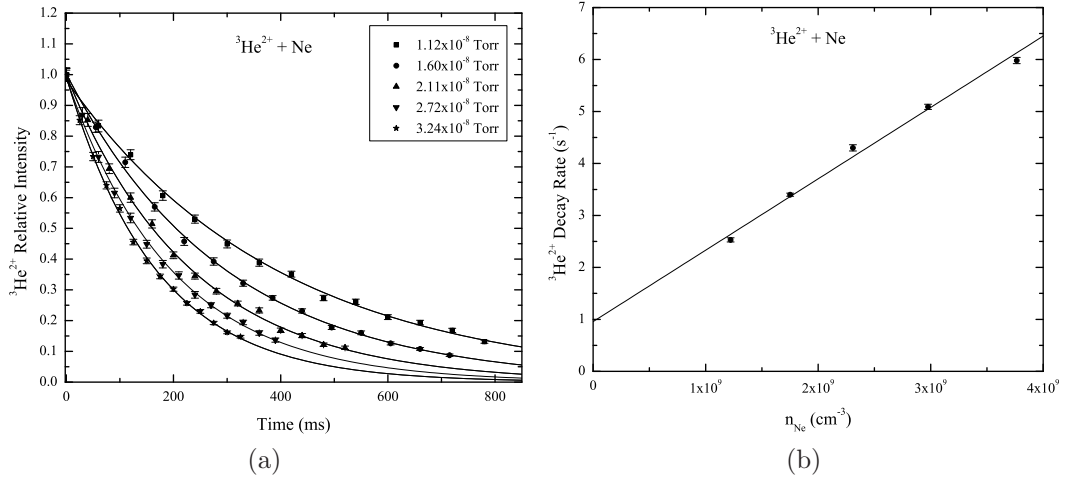


Figure 5.6: The  ${}^3\text{He}^{2+}$  ion population decay under different Ne pressures, (a), and the corresponding decay rates plotted against Ne number densities, (b).

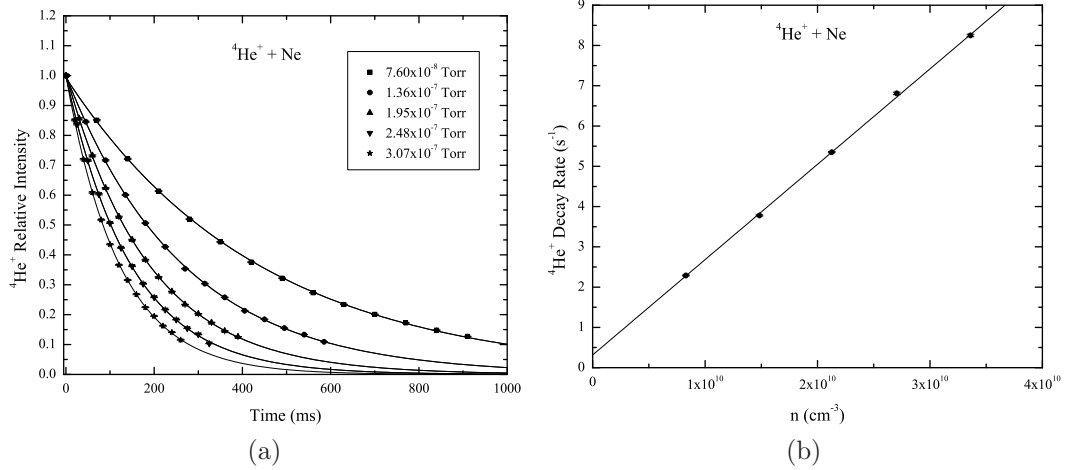


Figure 5.7: The  ${}^4\text{He}^+$  ion population decay under different Ne pressures, (a), and the corresponding decay rates plotted against Ne number densities, (b).

${}^4\text{He}^+$  has a small rate coefficient when reacting with Ne. A value of  $1.20 \pm 0.36 \times 10^{-15} \text{cm}^{-3} \text{s}^{-1}$  is recorded elsewhere [65].  ${}^4\text{He}^+$  is also subjected to the same trapping conditions as  ${}^3\text{He}^{2+}$  was. The leak rate coefficient obtained for the  ${}^4\text{He}^+$ -Ne reaction is  $2.37 \pm 0.24 \times 10^{-10} \text{cm}^{-3} \text{s}^{-1}$ , figure 5.7. A full five orders of magnitude larger than the measured charge transfer rate coefficient of  ${}^4\text{He}^+$ -Ne. Correcting for the leak rate coefficient caused by elastic collisions the sum of SCT and DCT rate coefficients of  ${}^3\text{He}^{2+}$  with Ne is  $1.13 \pm 0.16 \times 10^{-9} \text{cm}^{-3} \text{s}^{-1}$ .

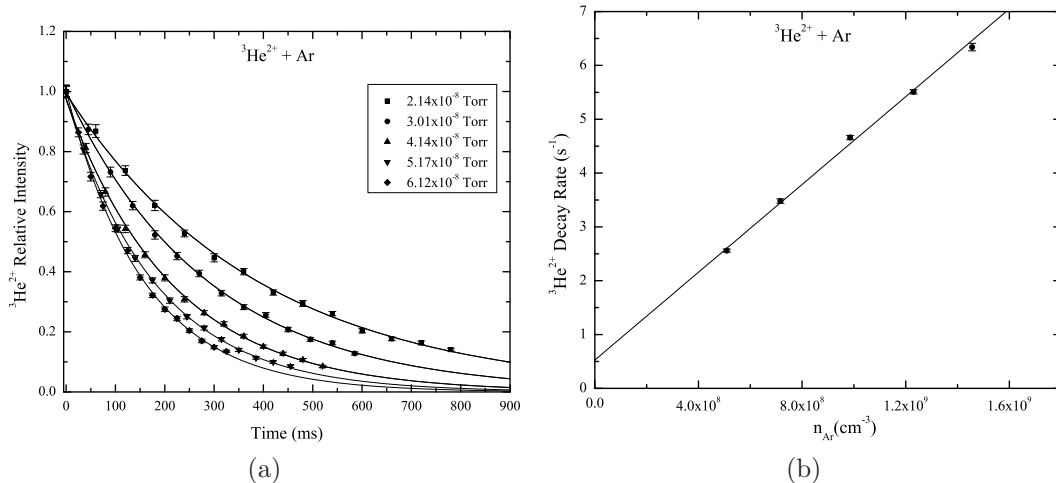


Figure 5.8: The  ${}^3\text{He}^{2+}$  ion population decay under different Ar pressures, (a), and the corresponding decay rates plotted against Ar number densities, (b).

Argon is treated in a similar fashion to the neon measurements. The Ar used for the charge transfer rate coefficient measurements and leak rate coefficient measurements was of 99.999% purity (Scott Specialty Gases INC.). QMS scans of the gas confirmed its purity no measurable elements other than Ar its isotopes and its doubly charged isotopes are detected. The uncorrected leak rate coefficient value is  $4.08 \pm 0.27 \times 10^{-9} \text{cm}^{-3} \text{s}^{-1}$ . Argon is also very slow to react with  ${}^4\text{He}^+$ ,  $\leq 1.00 \times 10^{-13} \text{cm}^{-3} \text{s}^{-1}$  [66], making the Ar- ${}^4\text{He}^+$  ideal to measure the leak rate coefficient caused by elastic collisions. The measured rate coefficient for Ar- ${}^4\text{He}^+$  was  $3.52 \pm 0.21 \times 10^{-10} \text{cm}^{-3} \text{s}^{-1}$ . Therefore the corrected sum of DCT and SCT rate coefficients for  ${}^3\text{He}^{2+}$ -Ar is  $3.73 \pm 0.27 \times 10^{-9} \text{cm}^{-3} \text{s}^{-1}$ .

The  ${}^3\text{He}^{2+}$  charge transfer rate coefficients with Krypton are also obtained through loss rates of  ${}^3\text{He}^{2+}$  plotted against their Kr number densities. Corrections for leak rates due to elastic collisions are also applied. The Krypton used was of 99.995% purity (Praxair INC.) and QMS scans revealed some concentration of  $m/q=28$  at 0.01% possibly nitrogen. The uncorrected rate coefficient is  $4.46 \pm 0.46 \times 10^{-9} \text{cm}^{-3} \text{s}^{-1}$ .

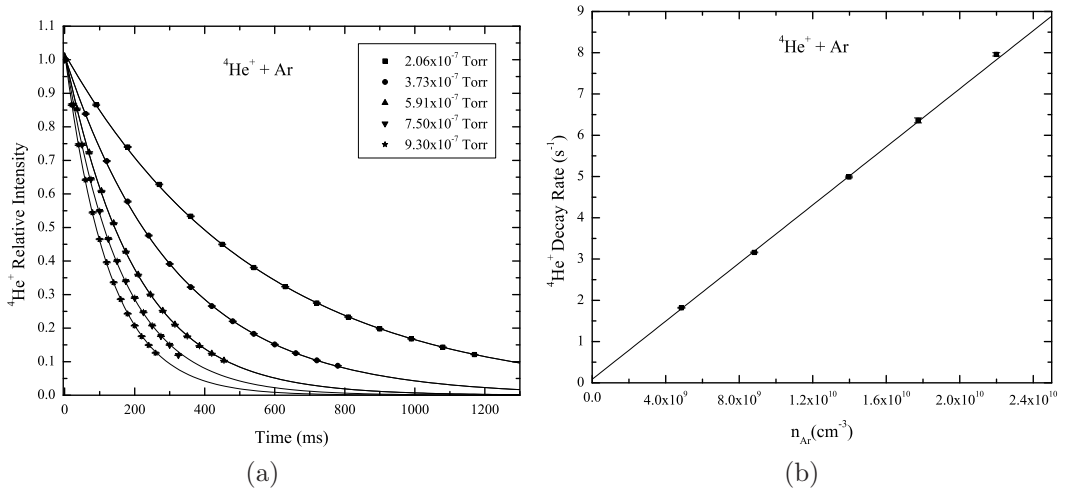


Figure 5.9: The  ${}^4\text{He}^+$  ion population decay under different Ar pressures, (a), and the corresponding decay rates plotted against Ar number densities, (b).

The leak rate coefficient, using  ${}^4\text{He}^+$  again, was  $4.39 \pm 0.44 \times 10^{-10} \text{ cm}^{-3} \text{ s}^{-1}$ . The corrected value for the DCT and SCT rate coefficients is therefore  $4.02 \pm 0.46 \times 10^{-9} \text{ cm}^{-3} \text{ s}^{-1}$ .

A full second set of measurements with leak corrections is also performed, to confirm that the charge transfer rate coefficients are independent of the  ${}^3\text{He}^{2+}$  location in the stability diagram. To achieve that the third and last set of trapping parameters is changed to 1.463 MHz,  $V_0$  at 91 V and  $U_0$  at 6.82 V. That placed the ion to the right of its original position. The corrected rate coefficient value is found to be  $4.17 \pm 0.49 \times 10^{-9} \text{ cm}^{-3} \text{ s}^{-1}$ , in good agreement with the value found when the ion is at its original stability diagram location.

Ultra high purity, 99.999%, Xenon was used in the measurements with  ${}^3\text{He}^{2+}$ . QMS scans of the xenon gas showed a clean gas in agreement with the prescribed purity. The rate coefficients are also corrected for the leak rate coefficient, caused by elastic collisions of  $\text{Xe}-{}^3\text{He}^{2+}$ . Because of its relative inertness with Xe,  ${}^4\text{He}^+$  is

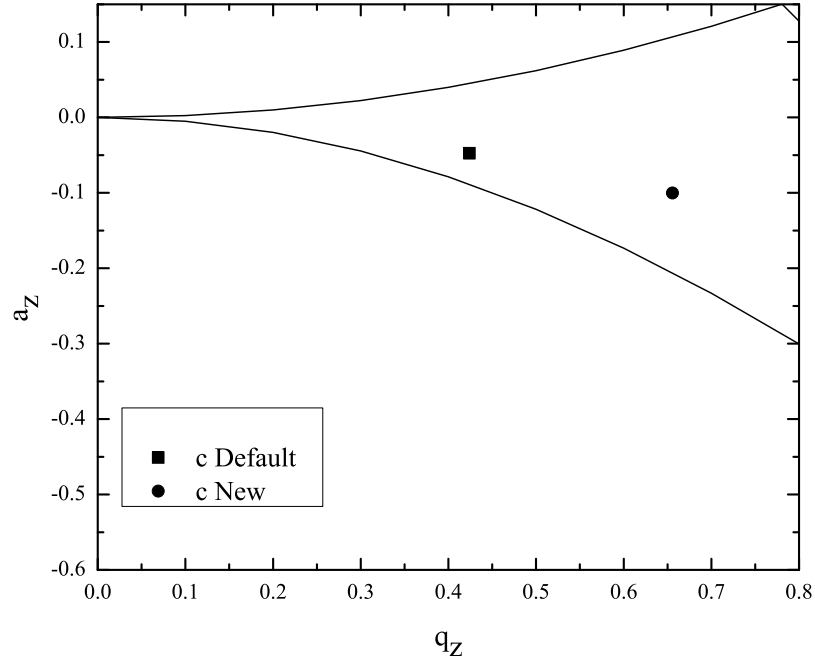


Figure 5.10: The  ${}^3\text{He}^{2+}$  ion shown in its third and last trapping condition  $c$  used to measure rate coefficients with the rest of noble and non noble gases. The two conditions,  $a$  and  $b$ , that preceded it were similar to the ones used in  ${}^3\text{He}^{2+}$ -He interactions, figure 5.2. The default location  $c$  corresponds to  $f=1.473$  MHz  $V_0=57$  V and  $U_0=3.3$  V. The new location  $c$  is used to investigate whether there is a location dependency in the rate coefficient and has  $f=1.463$  MHz  $V_0=90$  V and  $U_0=6.87$  V. The gases used to repeat the measurement at the new  $c$  location are Kr and Xe.

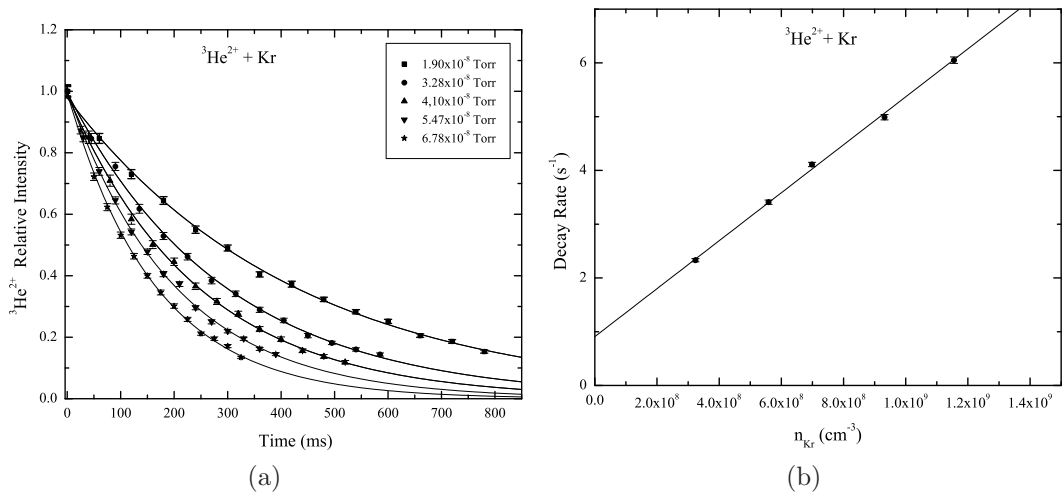


Figure 5.11: The  ${}^3\text{He}^{2+}$  ion population decay under different Kr pressures, (a), and the corresponding decay rates plotted against Kr number densities, (b).

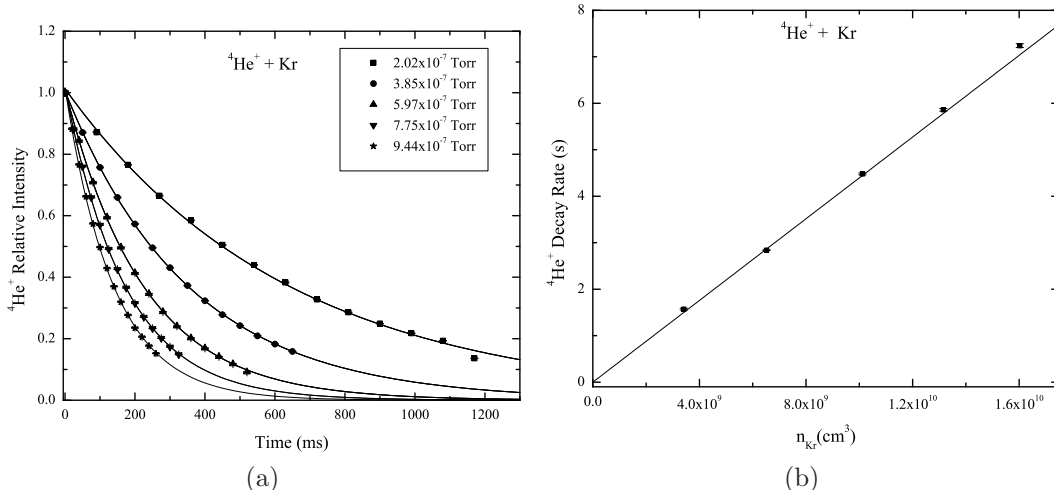


Figure 5.12: The  ${}^4\text{He}^+$  ion population decay under different Kr pressures, (a), and the corresponding decay rates plotted against Kr number densities, (b).

also used. The highest published value of charge transfer rate coefficients between  ${}^4\text{He}^+$ -Xe is  $7.00 \pm 1.4 \times 10^{-12} \text{cm}^{-3} \text{s}^{-1}$  [67]. The rate coefficient for DCT and SCT, uncorrected for leaks, is at  $7.01 \pm 0.71 \times 10^{-9} \text{cm}^{-3} \text{s}^{-1}$ . The leak rate coefficient is measured at  $8.98 \pm 1.09 \times 10^{-10} \text{cm}^{-3} \text{s}^{-1}$ , which yielded a corrected DCT and SCT rate coefficient of  $6.11 \pm 0.72 \times 10^{-9} \text{cm}^{-3} \text{s}^{-1}$ . The charge transfer rate coefficients dependency on well depth/stability diagram location was also explored, in  ${}^3\text{He}^{2+}$ -Xe reactions. One more full set is acquired with location to the right of the original ion coordinates in the stability diagram. The corrected value for DCT and SCT using the different trapping parameters was  $6.39 \pm 0.76 \times 10^{-9} \text{cm}^{-3} \text{s}^{-1}$ . This value is also in good agreement with the rate coefficient obtained using the default trapping values.

#### Section IV: $\text{He}^{2+}$ with $\text{H}_2$ , $\text{D}_2$ , $\text{CH}_4$ , $\text{N}_2$ and $\text{CO}$

By using the same experimental arrangement described in the measurements with the rest of the nobles, the rate coefficients for single and double charge transfer of  $\text{H}_2$ ,

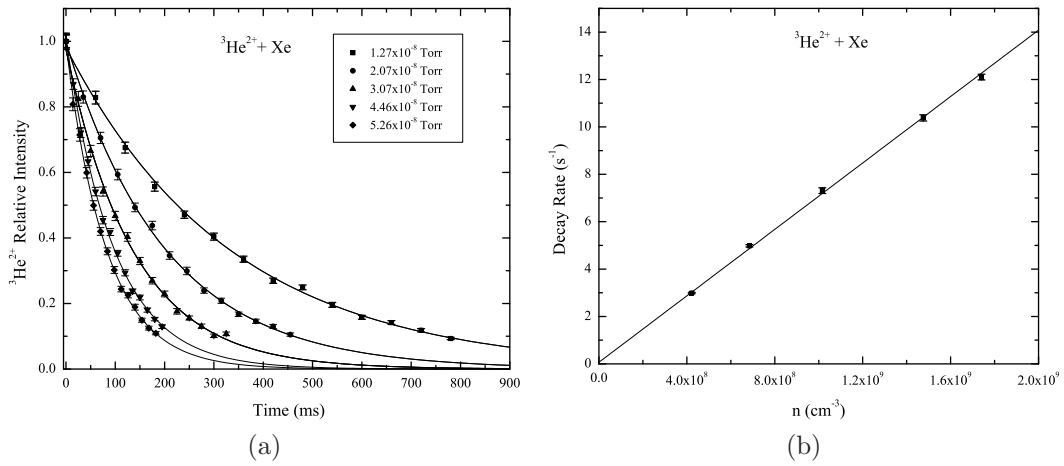


Figure 5.13: The  ${}^3\text{He}^{2+}$  ion population decay under different Xe pressures, (a), and the corresponding decay rates plotted against Xe number densities, (b).

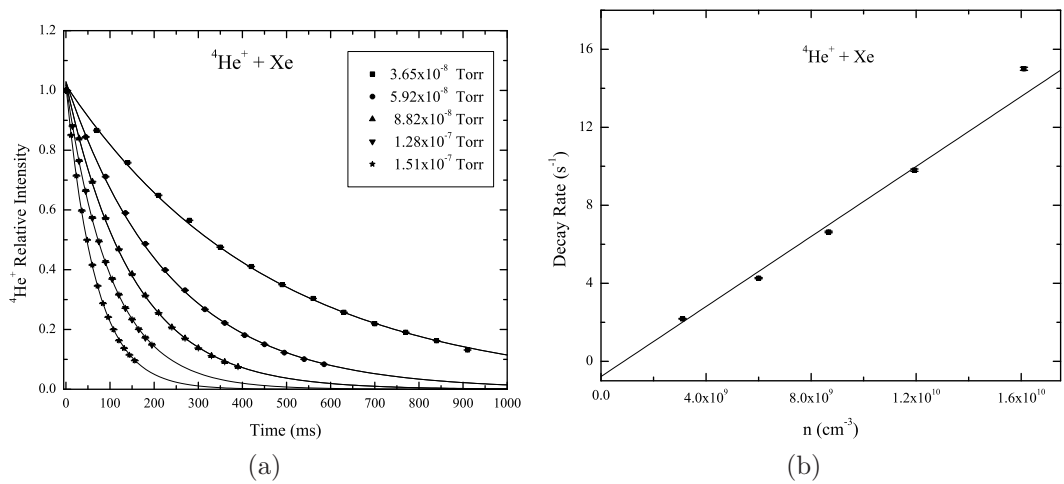


Figure 5.14: The  ${}^4\text{He}^+$  ion population decay under different Xe pressures, (a), and the corresponding decay rates plotted against Xe number densities, (b).



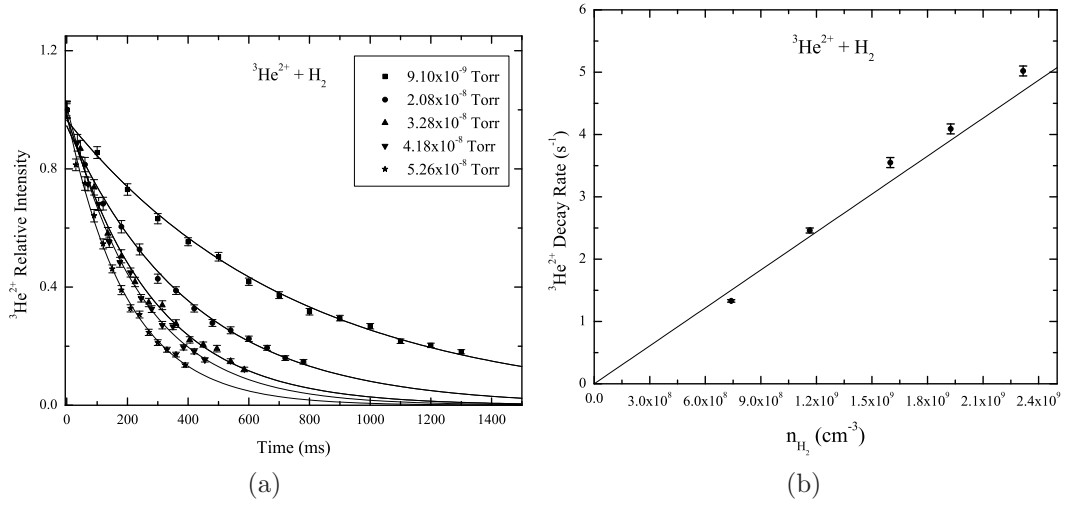
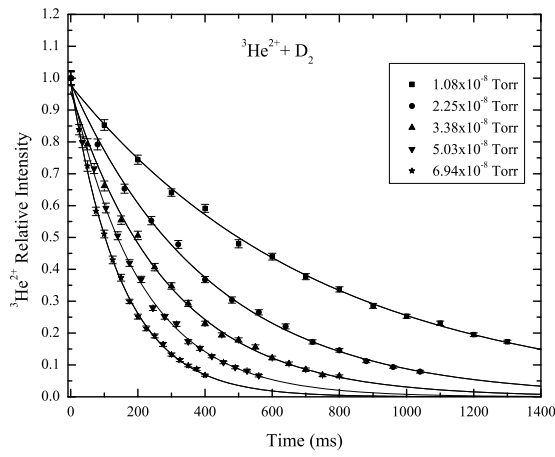


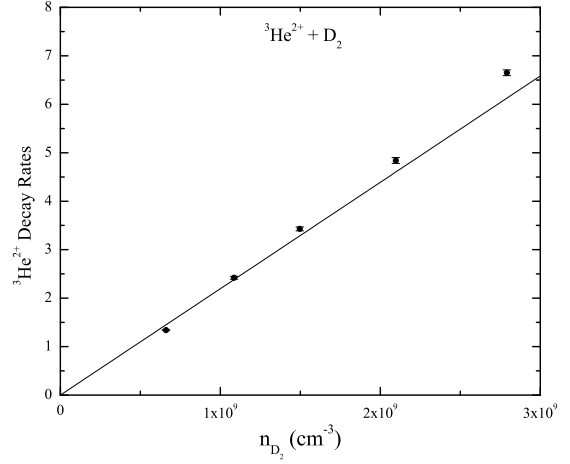
Figure 5.15: The  ${}^3\text{He}^{2+}$  ion population decay under different  $\text{H}_2$  pressures, (a), and the corresponding decay rates plotted against  $\text{H}_2$  number densities, (b).

$\text{D}_2$ ,  $\text{CH}_4$ ,  $\text{N}_2$  and  $\text{CO}$  with  ${}^3\text{He}^{2+}$ , as well as the leak rate coefficient due to elastic collisions are measured. The gases used are  $\text{H}_2$  99.999% (Linde),  $\text{D}_2$  99.8 % (Linde),  $\text{CH}_4$  99.999% (Air Gas INC),  $\text{N}_2$  99.999 % (Praxair), and  $\text{CO}$  99.99% (Air Gas INC). With the exception of  $\text{H}_2$  and  $\text{D}_2$ , where ionizing scans erroneously indicate increase in water and hydrocarbons, all other gases are within specifications.

The leak rate coefficient caused by elastic collision rf heating induced cannot be measured directly by interactions of non-noble gases with  ${}^4\text{He}^+$ . With the exception of  $\text{H}_2$  and  $\text{D}_2$ ,  $k \leq 10^{-13} \text{ cm}^3\text{s}^{-1}$  [68, 69],  ${}^4\text{He}^+$  will charge transfer readily with  $\text{CH}_4$ ,  $\text{N}_2$  or  $\text{CO}$ . Any loss rate of  ${}^4\text{He}^+$  population will be caused by charge transfer and not elastic collisions. However, using the leak rate coefficients measured in the noble gases a leak correction can be performed. The leak rate coefficient cross section has  $\alpha^{\frac{1}{2}}$  dependency. Therefore, the leak rate coefficient for  $\text{CH}_4$  can be obtained by using leak rate coefficient for  $\text{Ne}$  and correcting for the polarizability of  $\text{CH}_4$ . The leak rate for  $\text{He}^+$ - $\text{Ne}$  collisions is at  $2.37 \pm 0.24 \times 10^{-10} \text{ cm}^{-3}\text{s}^{-1}$ . The polarizability of  $\text{He}$  is

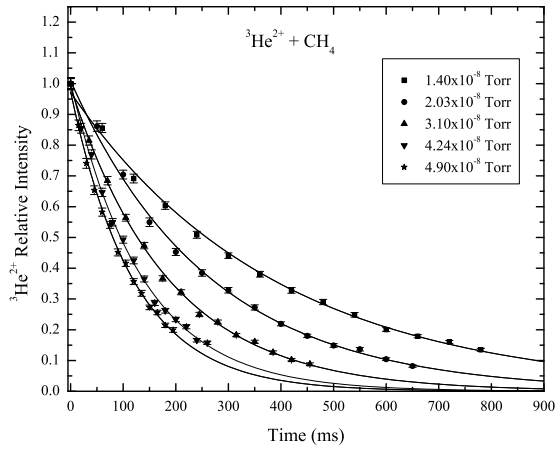


(a)

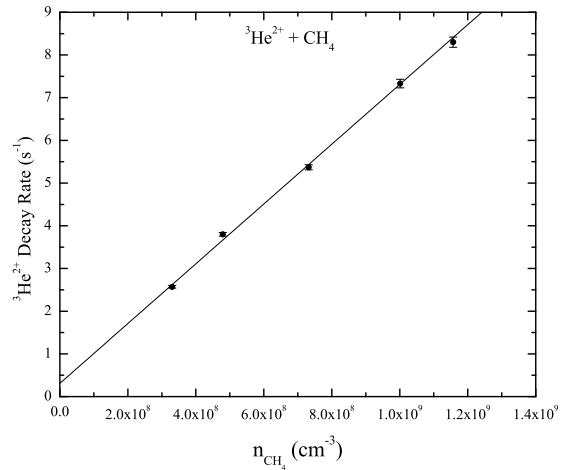


(b)

Figure 5.16: The  ${}^3\text{He}^{2+}$  ion population decay under different  $\text{D}_2$  pressures, (a), and the corresponding decay rates plotted against  $\text{D}_2$  number densities, (b).



(a)



(b)

Figure 5.17: The  ${}^3\text{He}^{2+}$  ion population decay under different  $\text{CH}_4$  pressures, (a), and the corresponding decay rates plotted against  $\text{CH}_4$  number densities, (b).

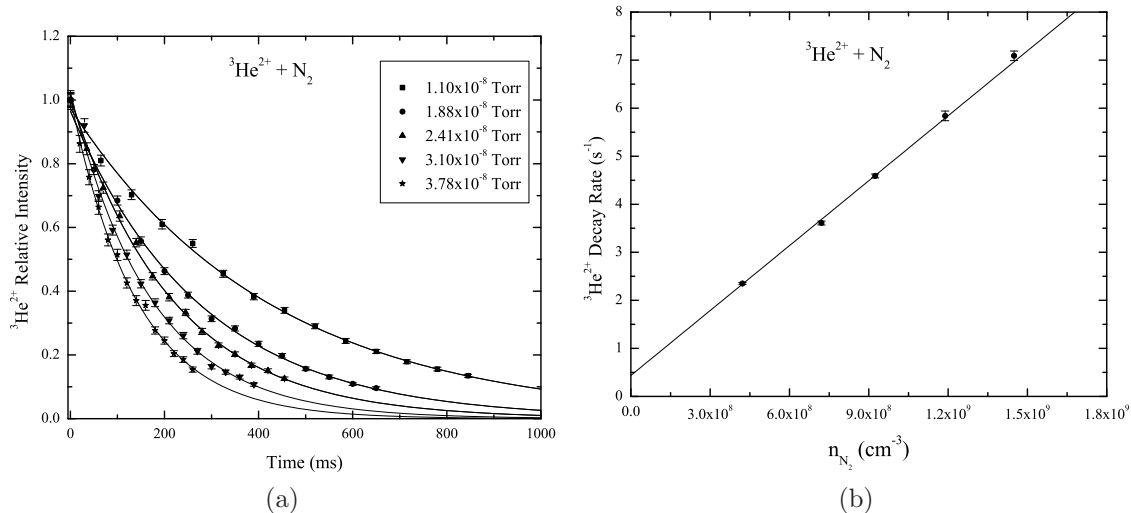


Figure 5.18: The  ${}^3\text{He}^{2+}$  ion population decay under different  $\text{N}_2$  pressures, (a), and the corresponding decay rates plotted against  $\text{N}_2$  number densities, (b).

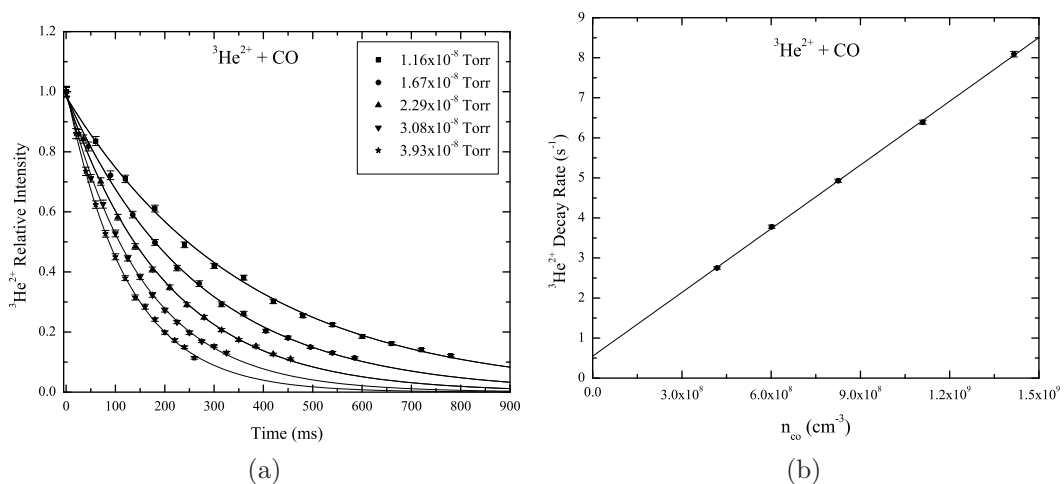


Figure 5.19: The  ${}^3\text{He}^{2+}$  ion population decay under different  $\text{CO}$  pressures, (a), and the corresponding decay rates plotted against  $\text{CO}$  number densities, (b).

$0.20 \times 10^{-24} \text{cm}^3$  the polarizability of  $\text{CH}_4$  is  $2.59 \times 10^{-24} \text{cm}^3$ . The corrected leak rate coefficient for  $\text{CH}_4$  will be  $6.06 \times 10^{-11} \text{cm}^{-3} \text{s}^{-1}$ . In a similar fashion, argon's leak rate coefficient can be used for calculating the leak rate of  ${}^3\text{He}^{2+}$  out of the ion trap through elastic collisions with CO and  $\text{N}_2$ .

## CHAPTER 6

### CONCLUSIONS

The deuterium abstraction and deuterium substitution in water ions and hydronium ions respectively may help improve the model of fractionation of water,  $[\text{HDO}]/[\text{H}_2\text{O}]$ , in planetary atmospheres, ISM, and cometary atmospheres. The measurement may resolve the discrepancy of observed against calculated fractionation ratio. In this work the rate coefficient of deuterium abstraction in water was measured at  $5.76 \pm 0.74 \times 10^{-10} \text{ cm}^3 \text{ s}^{-1}$  while the rate of deuterium substitution in hydronium ion  $\leq 5.88 \pm 1.50 \times 10^{-13} \text{ cm}^3 \text{ s}^{-1}$ .

$\alpha$ -particles,  $\text{He}^{2+}$ , can be found in solar winds and cosmic radiation and are also the ash in nuclear fusion occurring in plasma confinement type reactors. They can charge transfer with most neutrals. Charge transfer with neutral found in fusion reactors can lead to cooling of the plasma and failure of the fusion reaction. Charge transfer of  $\text{He}^{2+}$  with He and  $\text{H}_2$  is also of interest to astrophysics. Very little work exists in the 1-30 eV range in this work the gap of rate coefficients of charge transfer at low energies is filled. The resonant charge transfer coefficients of  $\text{He}^{2+}$  with He, the sum of single and double charge transfer rate coefficients of  $\text{He}^{2+}$  with the rest of the nobles, except radon, and the sum of single and double charge transfer rate coefficients of  $\text{He}^{2+}$  with  $\text{H}_2$ ,  $\text{D}_2$ ,  $\text{CH}_4$ ,  $\text{N}_2$  and  $\text{CO}$ , at energies of 0.24 eV, have been measured experimentally. Because of the trapped ion's smaller mass, compared to the interacting neutrals, corrections for losses due to collision induced rf heating were applied. The rate coefficients for charge transfer with Kr and Xe were measured again

Neutral	Rate Coefficient( $\text{cm}^3\text{s}^{-1}$ ) (This work)	Rate Coefficient ( $\text{cm}^3\text{s}^{-1}$ )
He	$5.92 \pm 0.58 \times 10^{-10}$ $\blacklozenge$	N/A
Ne	$1.13 \pm 0.16 \times 10^{-9}$ $\blacktriangle$	$8.4 \pm 2.0 \times 10^{-10}$ $\star$ [63]
Ar	$3.73 \pm 0.27 \times 10^{-9}$ $\blacktriangle$	$2.6 \pm 0.5 \times 10^{-9}$ $\star$ [63]
Kr	$4.02 \pm 0.46 \times 10^{-9}$ $\blacktriangle$	$3.9 \pm 0.6 \times 10^{-9}$ $\star$ [63]
Xe	$6.11 \pm 0.72 \times 10^{-9}$ $\blacktriangle$	$4.7 \pm 0.7 \times 10^{-9}$ $\star$ [63]
H <sub>2</sub>	$1.94 \pm 0.18 \times 10^{-9}$ $\blacktriangle$	$2.7 \pm 0.2 \times 10^{-9}$ $\blacktriangle$ [70]
D <sub>2</sub>	$2.10 \pm 0.19 \times 10^{-9}$ $\blacktriangle$	N/A
CH <sub>4</sub>	$6.39 \pm 0.74 \times 10^{-9}$ $\blacktriangle$	N/A
N <sub>2</sub>	$4.15 \pm 0.28 \times 10^{-9}$ $\blacktriangle$	$3.5 \pm 0.3 \times 10^{-9}$ $\blacktriangle$ [70]
CO	$4.92 \pm 0.33 \times 10^{-9}$ $\blacktriangle$	$3.5 \pm 0.3 \times 10^{-9}$ $\blacktriangle$ [70]

Table 6.1: All the He<sup>2+</sup> results performed in this work compared, whenever available, to results from the literature under similar energy range .  $\blacklozenge$  Double or resonant charge transfer only.  $\blacktriangle$  The sum of single and double charge transfer rate coefficients.  $\star$  Single charge transfer only.

using different trapping parameters to place the ion at a higher pseudopotential well, figure 5.10. Kr and Xe were chosen because they were the two most massive of the gases used. Should any discrepancy in the measurement under two different trapping conditions exists, it will be enhanced the most when the two heaviest gases are used. The results showed that the measured rate coefficients were invariant to the trapped ion's pseudopotential well, or location in the stability diagram. A table with the leak corrected charge transfer rate coefficients as well as experimental results from other work under similar energy conditions is attached.

## APPENDIX

### List of Abbreviations

CIT	Cylindrical Ion Trap
DCT	Double Charge Transfer
EII	Electron Impact Ionization
FSK	Frequency Shifting Key
ISM	Interstellar Medium
MCP	Micro Chanel Plate
QMS	Quadrupole Mass Spectrometer
RCT	Resonant Charge Transfer
RP	Resolving Power
SCT	Single Charge Transfer
TOF	Time of Flight

## BIBLIOGRAPHY

- [1] Gerin, M., De Luca, M., Black, J., Goicoechea, J. R., Herbst, E., Neufeld, D. A., Falgarone, E., Godard, B., Pearson, J. C., Lis, D. C., Phillips, T. G., Bell, T. A., Sonnentrucker, P., Boulanger, F., Cernicharo, J., Coutens, A., Dartois, E., Encrenaz, P., Giesen, T., Goldsmith, P. F., Gupta, H., Gry, C., Hennebelle, P., Hily-Blant, P., Joblin, C., Kazmierczak, M., Kolos, R., Krelowski, J., Martin-Pintado, J., Monje, R., Mookerjea, B., Perault, M., Persson, C., Plume, R., Rimmer, P. B., Salez, M., Schmidt, M., Stutzki, J., Teyssier, D., Vastel, C., Yu, S., Contursi, A., Menten, K., Geballe, T., Schlemmer, S., Shipman, R., Tielens, A., Philipp-May, S., Cros, A., Zmuidzinas, J., Samoska, L. A., Klein, K., and Lorenzani, A. (2010) *Astron. Astrophys.* **518**, 5.
- [2] Gupta, H., Rimmer, P., Pearson, J. C., Yu, S., Herbst, E., Harada, N., Bergin, E. A., Neufeld, D. A., Melnick, G. J., Bachiller, R., Baechtold, W., Bell, T. A., Blake, G. A., Caux, E., Ceccarelli, C., Cernicharo, J., Chattopadhyay, G., Comito, C., Cabrit, S., Crockett, N. R., Daniel, F., Falgarone, E., Diez-Gonzalez, M. C., Dubernet, M. L., Erickson, N., Emprechtinger, M., Encrenaz, P., Gerin, M., Gill, J. J., Giesen, T. F., Goicoechea, J. R., Goldsmith, P. F., Joblin, C., Johnstone, D., Langer, W. D., Larsson, B., Latter, W. B., Lin, R. H., Lis, D. C., Liseau, R., Lord, S. D., Maiwald, F. W., Maret, S., Martin, P. G., Martin-Pintado, J., Menten, K. M., Morris, P., Muller, H. S. P., Murphy, J. A., Nordh, L. H., Olberg, M., Ossenkopf, V., Pagani, L., Perault, M., Phillips, T. G., Plume, R., Qin, S. L., Salez, M., Samoska, L. A., Schilke, P., Schlecht, E., Schlemmer, S., Szczerba, R., Stutzki, J., Trappe, N., van derTak, F. F. S., Vastel, C., Wang, S., Yorke, H. W., Zmuidzinas, J., Boogert, A., Gusten, R., Hartogh, P., Honingh, N., Karpov, A., Kooi, J., Krieg, J. M., Schieder, R., and Zaal, P. (2010) *Astron. Astrophys.* **521**, 5.
- [3] Ossenkopf, V., Muller, H. S. P., Lis, D. C., Schilke, P., Bell, T. A., Bruderer, S., Bergin, E., Ceccarelli, C., Comito, C., Stutzki, J., Bacman, A., Baudry, A., Benz, A. O., Benedettini, M., Berne, O., Blake, G., Boogert, A., Bottinelli, S., Boulanger, F., Cabrit, S., Caselli, P., Caux, E., Cernicharo, J., Codella, C., Coutens, A., Crimier, N., Crockett, N. R., Daniel, F., Demyk, K., Dieleman, P., Dominik, C., Dubernet, M. L., Emprechtinger, M., Encrenaz, P., Falgarone, E., France, K., Fuente, A., Gerin, M., Giesen, T. F., diGiorgio, A. M., Goicoechea, J. R., Goldsmith, P. F., Gusten, R., Harris, A., Helmich, F., Herbst, E., Hily-Blant, P., Jacobs, K., Jacq, T., Joblin, C., Johnstone, D., Kahane, C., Kama, M., Klein, T., Klotz, A., Kramer, C., Langer, W., Lefloch, B., Leinz, C., Lorenzani, A., Lord, S. D., Maret, S., Martin, P. G., Martin-Pintado, J., McCoey, C., Melchior, M., Melnick, G. J., Menten, K. M., Mookerjea, B., Morris, P., Murphy, J. A., Neufeld, D. A., Nisini, B., Pacheco, S., Pagani, L., Parise, B., Pearson, J. C., Perault, M., Phillips, T. G., Plume, R., Quin, S. L., Rizzo, R., Rollig, M., Salez, M., Saraceno, P., Schlemmer, S., Simon, R., Schuster, K., van derTak, F. F. S., Tielens, A., Teyssier, D., Trappe, N., Vastel, C., Viti, S., Wakelam,



- V., Walters, A., Wang, S., Whyborn, N., van derWiel, M., Yorke, H. W., et al. (2010) *Astron. Astrophys.* **518**, 5.
- [4] Dalgarno, A. (1993) *J. Chem. Soc. Faraday Trans.* **89(13)**, 2111–2117.
- [5] Dalgarno, A. and Lepp, S. December 1984 *Astrophys. J. Lett.* **287**, L47–L50.
- [6] Roberts, H., Herbst, E., and Millar, T. J. October 2002 *Mon. Not.R. Astron. Soc.* **336**, 283–290.
- [7] Roberts, H. and Millar, T. J. September 2000 *Astron. Astrophys.* **361**, 388–398.
- [8] Smith, D., Adams, N. G., and Alge, E. (1982) *J. Chem. Phys.* **77(3)**, 1261–1268.
- [9] Bockelee-Morvan, D., Gautier, D., Lis, D. C., Young, K., Keene, J., Phillips, T., Owen, T., Crovisier, J., Goldsmith, P. F., Bergin, E. A., Despois, D., and Wootten, A. May 1998 *Icarus* **133**, 147–162.
- [10] Meier, R., Owen, T. C., Matthews, H. E., Jewitt, D. C., Bockelee-Morvan, D., Biver, N., Crovisier, J., and Gautier, D. (1998) *Science* **279(5352)**, 842–844.
- [11] Brown, P. D. and Millar, T. J. April 1989 *Mon. Not. R. Astron. Soc.* **237**, 661–671.
- [12] Tielens, A. G. G. M. March 1983 *Astron. Astrophys.* **119**, 177–184.
- [13] Yung, Y. L. and Kass, D. M. (1998) *Science* **280(5369)**, 1545–1546.
- [14] Krasnopolsky, V. A., Mumma, M. J., and Gladstone, G. R. (1998) *Science* **280(5369)**, 1576–1580.
- [15] L  cluse, C. and Robert, F. July 1994 *Geochim. Cosmochim. AC.* **58**, 2927–2939.
- [16] Post, D. E. (1983) In F. Brouillard & J. W. McGowan, (ed.), NATO ASIB Proc. 83: Physics of Ion-Ion and Electron-Ion Collisions, : pp. 37–99.
- [17] Barnsden, B. H. and McDowell, M. R. C. (2003) Charge Exchange and Theory of Ion Atom Collisions, Oxford University Press, Oxford, England.
- [18] Ratkiewicz, R., Rucinski, D., and Ip, W. April 1990 *Astron. Astrophys.* **230**, 227–232.
- [19] Hberli, R. M., Gombosi, T. I., De Zeeuw, D. L., Combi, M. R., and Powell, K. G. (1997) *Science* **276(5314)**, 939–942.
- [20] Dennerl, K. November 2002 *Astron. Astroph.* **394**, 1119–1128.
- [21] Bodewits, D., Hoekstra, R., Seredyuk, B., McCullough, R. W., Jones, G. H., and Tielens, A. G. G. M. May 2006 *Astrophys. J.* **642**, 593–605.
- [22] Langevin, P. (1905) *Annal. De Chim. Phys.* **5**, 245–288.
- [23] Gioumousis, G. and Stevenson, D. P. (1958) *J. Chem. Phys.* **29(2)**, 294–299.

- [24] Su, T. and Bowers, M. T. (1973) *Int. J. Mass Spectrom. Ion Phys.* **12(4)**, 347 – 356.
- [25] Su, T. and Bowers, M. T. (1973) *J. Am. Chem. Soc.* **95(5)**, 1370–1373.
- [26] Su, T. and Bowers, M. T. (1973) *J. Chem. Phys.* **58(7)**, 3027–3037.
- [27] Ryufuku, H., Sasaki, K., and Watanabe, T. Mar 1980 *Phys. Rev. A* **21**, 745–750.
- [28] Kwong, V. H. S., Gibbons, T. T., Fang, Z., Jiang, J., Knocke, H., Jiang, Y., Ruger, B., Huang, S., Braganza, E., Clark, W., and Gardner, L. D. July 1990 *Rev. Sci. Instrum.* **61**, 1931–1939.
- [29] Kyriakides, C. and Kwong, V. H. S. Linearity test of the mcp detector unpublished (2012).
- [30] Jones, J. D. C., Birkinshaw, K., and Twiddy, N. D. (1981) *Chem. Phys. Lett.* **77(3)**, 484–488.
- [31] Fehsenfeld, F. C., Schmeltekopf, A. L., and Ferguson, E. E. (1967) *J. Chem. Phys.* **46(7)**, 2802–2808.
- [32] Kim, J. K., Theard, L. P., and W. T. Huntress, J. (1975) *J. Chem. Phys.* **62(1)**, 45–52.
- [33] Dotan, I., Lindinger, W., Rowe, B., Fahey, D. W., Fehsenfeld, F. C., and Albritton, D. L. (1980) *Chem. Phys. Lett.* **72(1)**, 67 – 70.
- [34] Huntress, W. T., McEwan, M. J., Karpas, Z., and Anicich, V. G. (1980) *Astrophys. J. Suppl. Ser.* **44(4)**, 481–488.
- [35] Adams, N. G., Smith, D., and Grief, D. (1978) *Int. J. Mass Spectrom. Ion Proc.* **26(4)**, 405–415.
- [36] Karpas, Z., Anicich, V. G., and Huntress, W. T. (1978) *Chem. Phys. Lett.* **59(1)**, 84–86.
- [37] Karpas, Z., Anicich, V., and Huntress, W. T. (1979) *J. Chem. Phys.* **70(6)**, 2877–2881.
- [38] Rakshit, A. B. (1982) *Int. J. Mass Spectrom. Ion Proc.* **41(3)**, 185–197.
- [39] Hansel, A., Richter, R., Lindinger, W., and Ferguson, E. E. (1989) *Int. J. Mass Spectrom. Ion Proc.* **94(3)**, 251–260.
- [40] Gerlich, D. and Schlemmer, S. (2002) *Planet. Space Sci.* **50(12-13)**, 1287 – 1297.
- [41] Millar, T. J., Bennett, A., and Herbst, E. May 1989 *Astrophys. J.* **340**, 906–920.
- [42] Anicich, V. G. and Huntress, W. T. (1986) *Astrophys. J. Suppl. Ser.* **62(3)**, 553–672.

- [43] Huntress, W. T. and Pinizzot.Rf (1973) *J. Chem. Phys.* **59(9)**, 4742–4756.
- [44] Fang, Z., Chen, D., and Kwong, V. H. S. (2000) *Phys. Rev. A* **62(4)**, 6.
- [45] Smith, D. and Adams, N. G. (1977) *Astrophys. J.* **217(3)**, 741–748.
- [46] Anicich, V. G. and Sen, A. D. (1998) *Int. J. Mass Spectrom.* **172(1-2)**, 1–14.
- [47] Ellefson, R. E., Moddeman, W. E., and Dylla, H. F. (1981) *J. Vac. Sci. Technol.* **18(3)**, 1062–1067.
- [48] Lindeman.E, Rozett, R. W., and Koski, W. S. (1972) *J. Chem. Phys.* **56(11)**, 5490–5492.
- [49] Reutt, J. E., Wang, L. S., Lee, Y. T., and Shirley, D. A. (1986) *J. Chem. Phys.* **85(12)**, 6928–6939.
- [50] Mohlmann, G. R., Bhutani, K. K., and Deheer, F. J. (1977) *Chem. Phys.* **21(1)**, 127–134.
- [51] Heninger, M., Lemaire, J., Mauclaire, G., Fenistein, S., Jullien, S., and Marx, R. (1994) *J. Chem. Phys.* **101(3)**, 1923–1929.
- [52] Weis, B., Carter, S., Rosmus, P., Werner, H. J., and Knowles, P. J. (1989) *J. Chem. Phys.* **91(5)**, 2818–2833.
- [53] Schauer, M. M., Jefferts, S. R., and Dunn, G. H. (1990) *Phys. Rev. A* **42(9)**, 5332–5337.
- [54] Rundel, R. D., Nitz, D. E., Smith, K. A., Geis, M. W., and Stebbings, R. F. (1979) *Phys. Rev. A* **19(1)**, 33–42.
- [55] Shah, M. B., Elliott, D. S., McCallion, P., and Gilbody, H. B. (1988) *J. Phys. B-At Mol Opt. Phys.* **21(15)**, 2751–2761.
- [56] Dehmelt, H. (1968) volume **3**, of *Advances in Atomic and Molecular Physics* pp. 53 – 72 Academic Press.
- [57] Knight, R. D. Lifetime of the metastable  $23S1$  in stored  $Li^+$  ions PhD thesis University of California Berkley (1979).
- [58] Church, D. A. and Dehmelt, H. G. (1969) *J. Appl. Phys.* **40(9)**, 3421–3424.
- [59] Knight, R. D. and Prior, M. H. (1979) *J. Appl. Phys.* **50(5)**, 3044–3049.
- [60] Ifflnder, R. and Werth, G. (1977) *Metrologia* **13(3)**, 167.
- [61] Chernyi, G. G., Losev, S. A., Macheret, S. O., and Potapkin, B. V. (2002) *Physical and Chemical Processes in Gas Dynamics*, American Institute of Aeronautics and Astronautics, Reston, Va.
- [62] Johnsen, R. and Biondi, M. A. (1978) *Phys. Rev. A* **18(3)**, 996–1003.

- [63] Johnsen, R. and Biondi, M. A. (1979) *Phys. Rev. A* **20(1)**, 87–97.
- [64] Cohen, J. S. and Bardsley, J. N. (1978) *Phys. Rev. A* **18(3)**, 1004–1008.
- [65] Johnsen, R. (1983) *Phys. Rev. A* **28(3)**, 1460–1468.
- [66] Fehsenfeld, G., Schmelze, A., Goldman, P. D., Schiff, H. I., and Ferguson, E. E. (1966) *J. Chem. Phys.* **44(11)**, 4087–4094.
- [67] Howorka, F., Kuen, I., Villinger, H., Lindinger, W., and Futrell, J. H. (1982) *Phys. Rev. A* **26(1)**, 93–104.
- [68] Smith, R. D., Smith, D. L., and Futrell, J. H. (1976) *Int J Mass Spectrom. Ion Proc.* **19(4)**, 369–394.
- [69] Johnsen, R. and Biondi, M. A. (1974) *J. Chem. Phys.* **61(5)**, 2112–2115.
- [70] Tosh, R. E. and Johnsen, R. (1993) *Int. J. Mass. Spectrom. Ion Proc.* **123(3)**, 193–203.

## CURRICULUM VITA

Department of Physics and Astronomy  
University of Nevada, Las Vegas

Chrysanthos Kyriakides

### Contact Information:

Work:(702) 895-1726

e-mail: athos2373@yahoo.com

### Degrees:

Bachelor of Science, Physics, 1996

Rutger, The State University of New Jersey , New Brunswick, New Jersey

Master of Science, Optical Sciences, 2000

University of Arizona, Tucson, Arizona

